Research supported by the
National Oceanic and Atmospheric Administration
under Grants NA67RJ0152 and NA37RJ0202.

THE DYNAMICS OF MCS MESOHIGHS AND WAKE LOWS

by

Patrick T. Haertel

Richard H. Johnson, PI

Colorado State University

DEPARTMENT OF ATMOSPHERIC SCIENCE

PAPER NO. 649

THE DYNAMICS OF MCS MESOHIGHS AND WAKE LOWS

by

Patrick T. Haertel

Department of Atmospheric Science
Colorado State University
Fort Collins, CO 80523

Spring 1998

Atmospheric Science Paper No. 649

ABSTRACT

THE DYNAMICS OF MCS MESOHIGHS AND WAKE LOWS

MCS mesohighs and wake lows were simulated using a simple dynamical system in which the only forcing was the lower-tropospheric cooling associated with stratiform precipitation, and the response consisted entirely of buoyancy waves. The simulated mesohighs and wake lows resemble those observed in nature–their thermodynamic and kinematic structures, their positions relative to the forcing, and their life cycles are all realistic. When the forcing was steady and moved at a constant speed the mesohigh-wake-low response quickly approached a steady state. The steady-state response to the stratiform forcing is shown to be more intense than that associated with convective forcing, because the buoyancy-wave speed of the former is closer to the speed at which MCS's move. I conclude that MCS mesohighs and wake lows are a quasi-steady-state buoyancy-wave response to the lower-tropospheric cooling associated with stratiform precipitation.

TABLE OF CONTENTS

LIST OF FIGURES

Chapter 1

INTRODUCTION

1.1 Background

Much of the springtime rain over the central United States comes from mesoscale convective systems (MCS's) that contain both vigorous convection and stratiform precipitation (Houze et al. 1990). Within these systems the convection is often confined to a propagating band or squall line which is trailed by the stratiform precipitation. Hereafter we refer to an MCS with this organization as a squall system. This paper discusses two surface-pressure features that occur frequently in squall systems and other MCS's–the mesohigh and the wake low (e.g. Fujita 1955, Pedgley 1962, Johnson and Hamilton 1988). Figure 1.1 shows their typical position in a mature squall system. The mesohigh lies beneath the convective line and the wake low trails the stratiform region. Mesohighs and wake lows are of more than academic interest. The intense pressure gradients which accompany them have been known to produce severe winds over land (Schmidt and Cotton 1989, Loehrer and Johnson 1995) and gale-force winds over water (Ely 1982), and they were probably responsible for severe wind shear which nearly caused a plane crash at Dallas-Fort Worth International Airport (Meuse et al. 1996).

Mesohighs and wake lows evolve during an MCS's lifetime. Using observations of several squall systems over the central United States, Fujita (1955, 1963) identified five stages in the life-cycle of a squall system and provided typical surface-pressure traces for each of these stages (Figure 1.2). Although these traces indicate how surface pressure changes with respect to time at a point fixed in space, for a system which evolves slowly as it passes the point the traces also approximate the spatial variation of surface pressure. A weak mesohigh forms during the *initiation stage,* and it grows larger than 100 km by the *development stage.* Showers reach their maximum intensity during the *mature stage* and the wake low forms behind them. During the *dissipation stage* the precipitation and the mesohigh diminish, but the wake low reaches its maximum intensity. Finally, the wake low fills during the *remnant stage.* Pedgley (1962) observed a similar life cycle within squall systems over Great Britain, and Johnson and Hamilton (1988) also observed a squall system whose surface-pressure features exhibited this life cycle.

The structure of surface pressure within MCS's is closely related to the pattern precipitation. Loehrer and Johnson (1995) examined this relationship for sixteen MCS's which passed over the central United States during May and June 1985. They constructed schemata for two radar-reflectivity patterns identified by Houze et al. (1990) (Figure 1.3). For the symmetric MCS the enhanced stratiform precipitation lies directly behind the convective line. For the asymmetric system the stratiform region is displaced to the left of the direction of propagation. For both systems the mesohigh lies ahead of the stratiform region, and the wake low trails the stratiform region.

Both the mesohigh and the wake low are primarily hydrostatic in nature. Above the mesohigh the lower troposphere is cool and dense (Fujita 1959, Johnson and Hamilton 1988, Smull and Jorgensen 1990) and its excess weight per area accounts for most of the pressure surplus (Fujita 1959). This coolness has been attributed to the evaporation, melting and sublimation of hydrometeors (Fujita 1959, Zhang and Gao 1989, Gallus 1996). While such phase changes of atmospheric water cool air locally, they also cause air parcels to become negatively buoyant, to descend, and to transport the coolness downward (e.g. Rotunno et al. 1988). Gallus and Johnson (1991) measured the net low-level cooling resulting from all of these processes both in the convective line and the stratiform region of a squall system. They found that while there was cooling in both places, the stratiform cooling was deeper and more intense. Other factors which may contribute to the mesohigh include the weight of hydrometeors (Sanders and Emanuel 1977) and dynamic pressure (Schaffer 1947).

Above the wake low the lower troposphere is warm, and its deficit in weight per area approximately equals the pressure deficit (Williams 1963, Johnson and Hamilton 1988, Johnson et al. 1989, Stumpf et al. 1991). The lower troposphere is usually also dry, so that profiles of temperature and dewpoint outline the shape of an onion (e.g. Figure 1.4). There is a consensus that the warmth and dryness result from subsidence, but researchers have differing ideas on the cause of this subsidence. Miller and Betts (1977) suggested that the subsidence is dynamically driven by the spreading of cool air near the surface. Johnson and Hamilton (1988) connected the subsidence to rear inflow into the system. Zhang and Gao (1989) called the wake low an "end product of a chain of complicated dynamic reactions" associated with latent cooling. Schmidt and Cotton (1990) attributed the subsidence and warming to buoyancy-wave (gravity-wave) circulations. Gallus (1996) showed that microphysical processes within the stratiform region alone could generate strong subsidence, but only when the precipitation rates were prescribed to decrease with time did the subsidence generate significant low-level warming. While these studies do not clarify the dynamics of wake lows, it is clear that stratiform precipitation plays an important role in their formation as is indicated by the schemata of Loehrer and Johnson (1995) (Figure 1.3).

1.2 Motivation

While previous studies have provided much information about MCS mesohighs and wake lows, their description of these surface-pressure features is still lacking. Not only do they fail to explain the dynamics of the wake low, they also leave questions pertaining to the mesohigh unanswered. For example, why is the maximum surface pressure found ahead of and not beneath the stratiform region where the low-level cooling is the most intense? It turns out that much of the structure of both the mesohigh and the wake low may be interpreted as a buoyancy-wave response to the low-level cooling produced by stratiform precipitation. This paper contains numerical simulations which illustrate this idea and a mathematical derivation of the mesohigh-wake-low response. Chapter 2 describes the dynamical system on which the numerical simulations are based, Chapter 3 discusses the simulations, Chapter 4 contains the derivation, and Chapter 5 summarizes this paper.

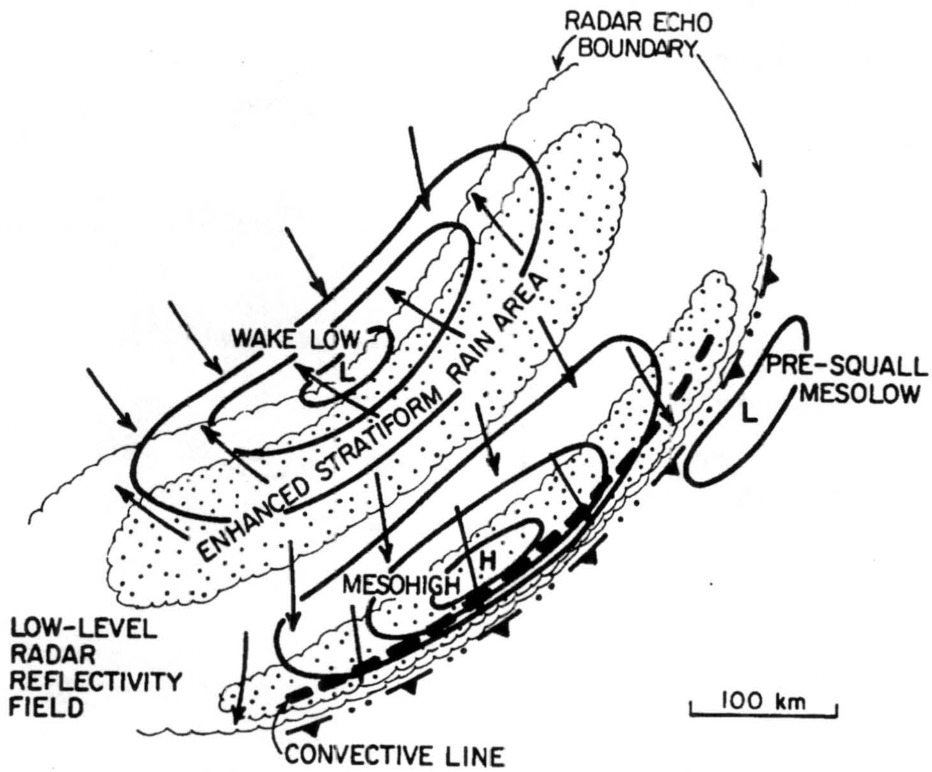

Figure 1.1. Schema of a mature squall system (from Johnson and Hamilton 1988). Surface pressure is contoured, vectors represent surface wind, and significant regions of precipitation are stippled.

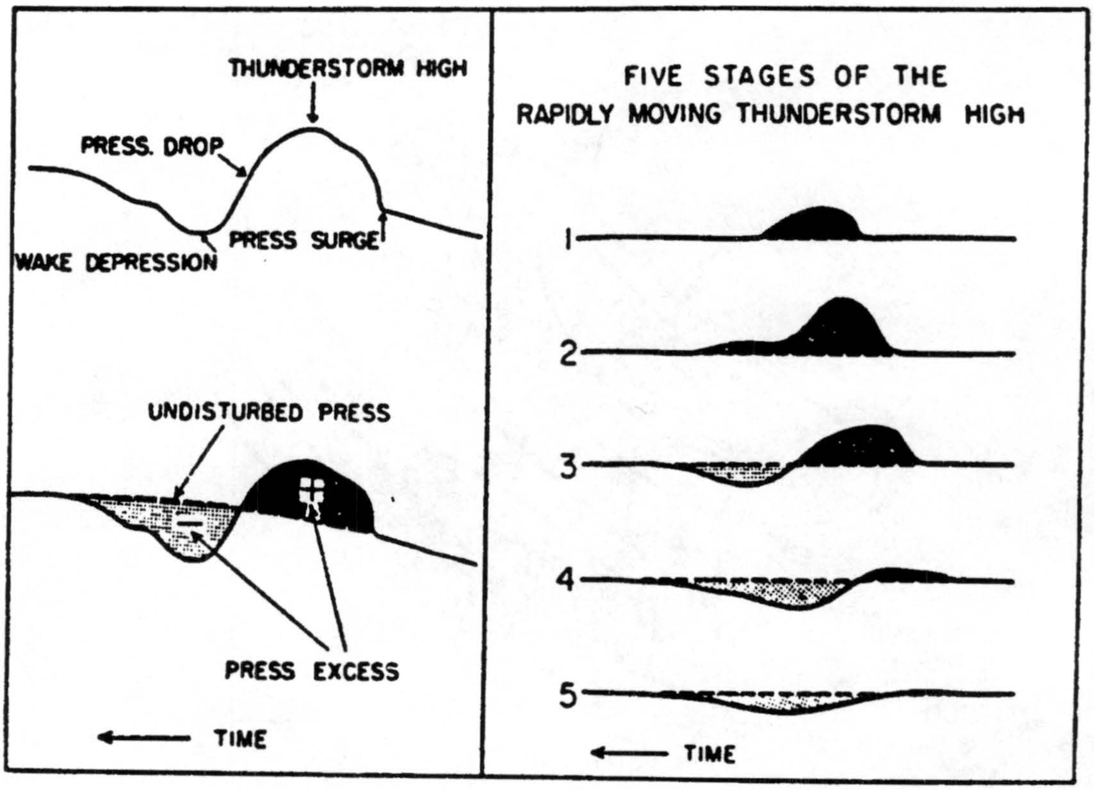

Figure 1.2. Surface-pressure traces for five stages of a squall system (from Fujita 1955). Stage 1 is the *initiation stage,* stage 2 is the *development stage,* stage 3 is the *mature stage,* stage 4 is the *dissipation stage* and stage 5 is the *remnant stage.*

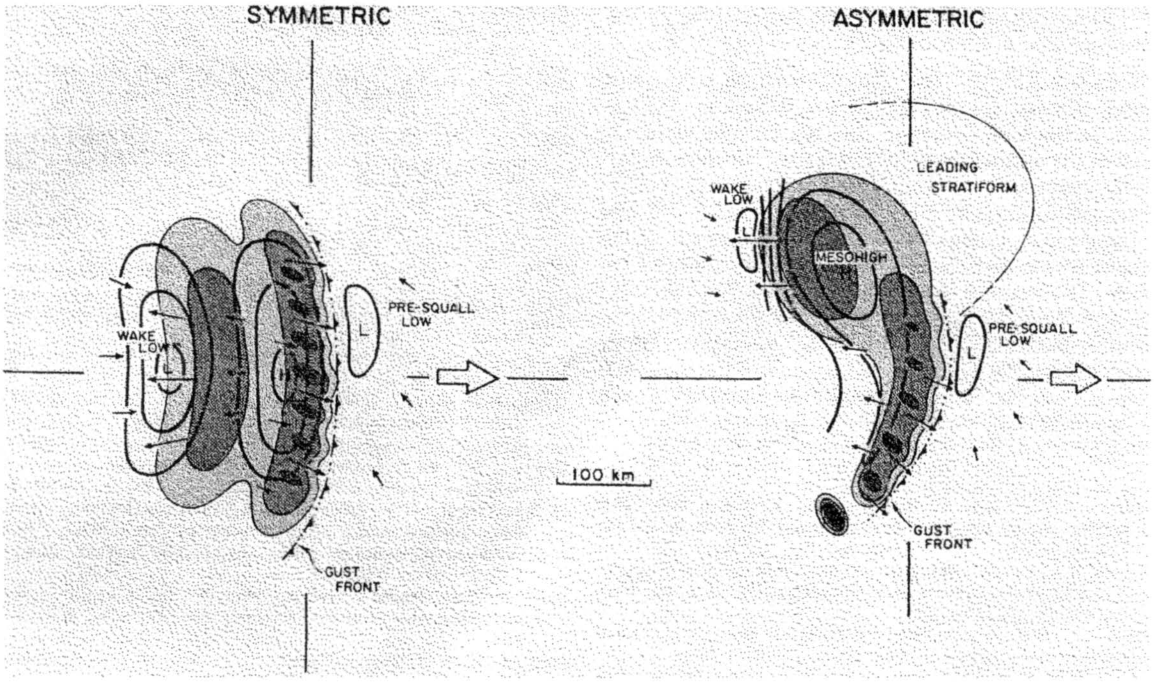

Figure 1.3. Schemata of symmetric and asymetric mesoscale convective systems. Levels of shading denote increasing radar reflectivity, surface pressure is contoured with a 1 hPa interval, and vectors represent surface winds (from Loehrer and Johnson 1995).

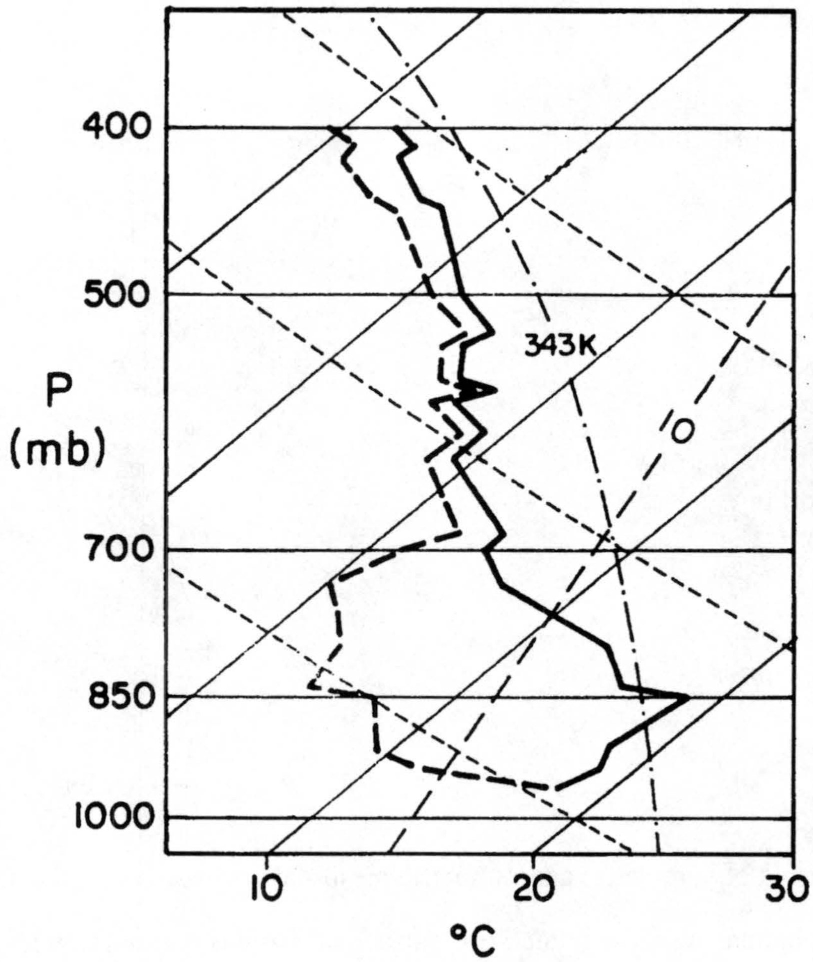

Figure 1.4. Temperature (solid) and dew point (dashed) above Wichita, Kansas at 0624 UTC 11 June 1985 (from Johnson and Hamilton 1988).

Chapter 2

THE DYNAMICAL SYSTEM

The numerical simulations presented in this paper are solutions to the irrotational Boussinesq equations linearized about a basic state of rest with a rigid upper boundary. This system, which was selected for its simplicity, supports simulations which are easily interpreted both physically and dynamically. It does, however, have several limitations that are discussed in this chapter. In order to illustrate these limitations we first carry out a preliminary simulation of the atmospheric response to the low-level cooling produced by stratiform precipitation, and then test the sensitivity of that response to modifications in the dynamical system.

2.1 A preliminary simulation

Consider the two-dimensional version of the system:

$$\frac{\partial u}{\partial t} + \frac{1}{\rho_0}\frac{\partial p}{\partial x} = 0 \tag{2.1}$$

$$\frac{1}{\rho_0}\frac{\partial p}{\partial z} = b \tag{2.2}$$

$$\frac{\partial b}{\partial t} + wN^2 = Q \tag{2.3}$$

$$\frac{\partial u}{\partial x} + \frac{\partial w}{\partial z} = 0 \tag{2.4}$$

where t is time, x denotes horizontal position, z is height, u and w are velocities in the x- and z-directions respectively, g is gravity, ρ_0 is density, p is perturbation pressure, b is perturbation bouyancy, N is the buoyancy frequency and Q is the thermal forcing. Having a rigid upper-boundary requires that $0 \le z \le H$ and that w vanishes at $z = 0$ and $z = H$ where H is the height of the boundary. We set $H = 4$ km, $N = 0.01\mathrm{s}^{-1}$ and $\rho_0 = 1.0$ kg m^{-3}.

We define the thermal forcing (Figure 2.1) to resemble the low-level cooling associated with the stratiform region of a squall system (e.g. Gallus and Johnson 1991):

$$Q(x, z, t) = Q_0\, Q_x(x) \sin(m_0 z)\, Q_t(t) \tag{2.5}$$

where $Q_0 = -1.99\ x\ 10^{-5} m\ s^{-3}$, $Q_x = \exp\left[-\left(\frac{x}{r}\right)^2\right]$, $m_0 = \frac{\pi}{H}$, $Q_t = 1$ for $t \le 2$ h and $Q_t = 0$ for $t > 2$ h, and $r = 75$ km. This forcing represents only a portion of the forcing associated with squall systems. Typically there is also heating through the depth of the troposphere in the vicinity of the convective line and heating in the upper troposphere in the stratiform region. These heatings appear to have less of an impact on surface-pressure structure within MCS's than stratiform cooling does. In Chapter 4 we discuss why the deep convective heating is less important. We neglect the upper-tropospheric stratiform heating because at least initially, the effects of this heating are confined to the upper-troposphere.

Before solving (2.1-2.4) we simplify the system algebraically. Combining (2.2-2.4) we eliminate b and w:

$$\frac{\partial}{\partial t}\frac{\partial^2 p}{\partial z^2} - \rho_0 N^2 \frac{\partial u}{\partial x} = \rho_0 \frac{\partial Q}{\partial z} \tag{2.6}$$

Next we assume that u and p have the following forms:

$$u(x, z, t) = -\hat{u}(x, t) \cos(m_0 z) \tag{2.7}$$

$$p(x, z, t) = -\hat{p}(x, t) \cos(m_0 z) \tag{2.8}$$

Substituting into (2.1) and (2.6) using (2.5) and (2.7-2.8) yields:

$$\frac{\partial \hat{u}}{\partial t} + \frac{1}{\rho_0} \frac{\partial \hat{p}}{\partial x} = 0 \tag{2.9}$$

$$\frac{\partial \hat{p}}{\partial t} + \frac{\rho_0 N^2}{{m_0}^2} \frac{\partial \hat{u}}{\partial x} = \frac{\rho_0}{m_0} \hat{Q} \tag{2.10}$$

where $\hat{Q}(x, t) = Q_0\, Q_x(x)\, Q_t(t)$. We further simplify (2.9-2.10) by defining the following non-dimensional variables:

$$x' = \frac{1}{[x]}\, x \tag{2.11}$$

$$t' = \frac{N}{m_0 [x]}\, t \tag{2.12}$$

$$\hat{u}' = \frac{m_0}{N}\, \hat{u} \tag{2.13}$$

$$\hat{p}' = \frac{{m_0}^2}{\rho_0 N^2}\, \hat{p} \tag{2.14}$$

$$\hat{Q}' = \frac{{m_0}^2 [x]}{N^3}\, \hat{Q} \tag{2.15}$$

where $[x]$ is an arbitrary unit of distance ([x] = 75 km for this section). Substituting (2.11-2.15) into (2.9-2.10) yields:

$$\frac{\partial \hat{u}'}{\partial t'} + \frac{\partial \hat{p}'}{\partial x'} = 0 \tag{2.16}$$

$$\frac{\partial \hat{p}'}{\partial t'} + \frac{\partial \hat{u}'}{\partial x'} = \hat{Q}' \tag{2.17}$$

We have reduced the system to the non-dimensional irrotational shallow water equations.

We solve (2.16-2.17) numerically using leapfrog time-differencing ($\Delta t' = 0.05$) and centered, forth-order spatial differencing ($\Delta x' = 0.1$). Using (2.2), (2.4), (2.7-2.8), (2.11-2.14) and the boundary condition for w at $z = 0$, we express solutions to (2.1-2.4) in terms of solutions to (2.16-2.17):

$$u = -\frac{\hat{u}' N}{m_0} \cos(m_0 z) \tag{2.18}$$

$$p = -\frac{\hat{p}' \rho_0 N^2}{{m_0}^2} \cos(m_0 z) \tag{2.19}$$

$$b = \frac{\hat{p}' N^2}{m_0} \sin(m_0 z) \tag{2.20}$$

$$w = \frac{N}{{m_0}^2 [x]} \frac{\partial \hat{u}'}{\partial x} \sin(m_0 z) \tag{2.21}$$

Notice that (2.21) is also consistent with the boundary condition for w at $z = H$.

The thermal forcing generates a cool anomaly with a matching vertical structure (Figure 2.2(a), top). After two hours of forcing this anomaly has grown to be 300 km across. When the forcing ends the anomaly divides in two, and each of the resulting anomalies propagate away (Figure 2.2(a), bottom). The perturbation pressure is positive below each cool anomaly and negative above each anomaly (Figure 2.2(b)). Before the forcing ends, the pressure gradient accelerates winds away from the forcing below 2 km and towards the forcing above 2 km (Figure 2.2(c), top). The forcing generates subsidence in its vicinity and a region of rising motion to each side of the subsidence

(Figure 2.2(d)).

The atmospheric response to the thermal forcing may be interpreted in terms of wave dynamics. The forcing generates two buoyancy-waves, one which propagates eastward and one which propagates westward. Within the eastward-propagating (westward-propagating) wave, the perturbation in pressure is in (π radians out of) phase with the perturbation in wind. Both waves have a phase speed of one non-dimensional unit of velocity, or 13 m s^{-1}.

2.2 Nonlinear terms

One of the limitations of the system (2.1-2.4) is that it neglects nonlinear terms which represent the advection of perturbation buoyancy and perturbation wind. In this section we estimate the magnitude that these terms would have in a nonlinear simulation.

The following two equations are nonlinear counterparts to (2.1) and (2.3):

$$\frac{\partial u}{\partial t} + u\frac{\partial u}{\partial x} + w\frac{\partial u}{\partial z} + \frac{1}{\rho_0}\frac{\partial p}{\partial x} = 0 \tag{2.22}$$

$$\frac{\partial b}{\partial t} + u\frac{\partial b}{\partial x} + w\frac{\partial b}{\partial z} + wN^2 = Q \tag{2.23}$$

Together with (2.2) and (2.4) these equations form a closed system. In deriving (2.23) we have assumed that the perturbation potential temperature is much smaller in magnitude than the basic state potential temperature. While the only way to rigorously test the importance of the nonlinear terms is to numerically solve these equations, we can calculate their magnitude within the preliminary simulation. Such a calculation shows to what extent the linear terms excite the nonlinear terms. After two hours of forcing the horizontal and vertical advection of perturbation wind each are about one-third as intense as the pressure gradient field (Figure 2.3). The vertical advection of perturbation bouyancy is also about one-third as intense as the vertical advection of the basic state buoyancy (Figure 2.4) whereas the horizontal advection of buoyancy is negligible (not shown).

Does neglecting nonlinear terms which have one-third the amplitude of the linear terms present a problem? Probably not. Since the nonlinear terms are relatively small they probably do not significantly change the interactions between the linear terms within the nonlinear system. In other words we expect the nonlinear system to support buoyancy waves similar to those seen in the preliminary simulation, and the linear simulation may be interpreted as a filtered version of the nonlinear simulation.

2.3 The upper boundary

A second limitation of the dynamical system is that it has a rigid upper boundary, unlike the real atmosphere which is unbounded. In this section we examine how removing this upper boundary alters the preliminary simulation.

In section 2.1 we reduced the dynamical system (2.1-2.4) to shallow water equations. This is possible when the thermal forcing has the form:

$$Q(x,z,t) = \hat{Q}(x,t)\sin(mz) \tag{2.24}$$

where $m = \dfrac{j\pi}{H}$ and j is an integer. This restriction on m forces w to vanish at the height of the rigid lid, so when the rigid lid is removed (2.1-2.4) may be reduced to shallow water equations when the forcing satisfies (2.24) and m is any real number. Hereafter we refer to a solution associated with a forcing which satisfies (2.24) as a vertical mode with wavenumber m. When the atmosphere is unbounded a thermal forcing which satisfies (2.24) is unrealistic; it does not vanish as $z \to \infty$. So how do we model the atmospheric response to a realistic forcing which vanishes above a certain height? We approximate the forcing as a sum of functions whose form is given by (2.24) and use shallow water equations to solve for the portion of the response associated with each term in the sum.

Consider the thermal forcing which is defined by (2.5) for $z \le H$ and is zero for $z > H$. Let $\tilde{Q}(z)$ denote the vertical structure of this forcing and let h be as follows:

$$h(z) = \begin{cases} \tilde{Q}(z) \text{ for } z \ge 0 \\ \\ -\tilde{Q}(-z) \text{ for } z < 0 \end{cases} \tag{2.25}$$

We rewrite h using a Fourier integral (Papoulis 1962):

$$h(z) = \frac{1}{2\pi} \int_{-\infty}^{\infty} \left\{ \int_{-\infty}^{\infty} e^{-imz'} \, h(z') \, dz' \right\} e^{imz} \, dm \tag{2.26}$$

Since h is an odd function (2.26) reduces to:

$$h(z) = \frac{2}{\pi} \int_{0}^{\infty} \left\{ \int_{0}^{\infty} \sin(mz') \, h(z') \, dz' \right\} \sin(mz) \, dm \tag{2.27}$$

We approximate the integrals in (2.27) with Riemann sums:

$$h(z) \approx \frac{2}{\pi} \sum_{j=1}^{\infty} \left\{ \sum_{k=1}^{\infty} \sin[(j\Delta m)(k\Delta z)] \, h(k\Delta z) \, \Delta z \right\} \sin[(j\Delta m)z] \, \Delta m \tag{2.28}$$

where Δm and Δz are small positive numbers. Noting that $h(z) = \tilde{Q}(z)$ for $z \ge 0$ we rewrite (2.28) obtaining the desired form for $\tilde{Q}$:

$$\tilde{Q}(z) \approx \sum_{j=1}^{\infty} a_j \sin[(j\Delta m)z] \tag{2.29}$$

where a_j is defined as follows:

$$a_j = \frac{2\Delta m}{\pi} \sum_{k=1}^{\infty} \sin[(j\Delta m)(k\Delta z)] \, h(k\Delta z) \, \Delta z \tag{2.30}$$

The accuracy of this approximation depends on Δm and Δz. For our purposes $\Delta m = \dfrac{m_0}{10}$

and $\Delta z = 20$ m and we retain 200 terms in the sum. The resulting approximation of $\tilde{Q}$ and a_j for $j = 1, 2, \ldots, 200$ are shown in Figure 2.5. Between 0 and 8 km the difference between the exact and approximate $\tilde{Q}$ is almost imperceptible. There are, however, significant errors near a height of 80 km and above. Because only a finite number of modes are included in the approximation, the approximate $\tilde{Q}$ is periodic with a wavelength of $\dfrac{2\pi}{\Delta m} = 80km$. These errors are not a concern to us, because their effects do not reach the lowest 8 km of the atmosphere during the simulation presented here.

We solve (2.1-2.4) by summing the solutions associated with each term of the sum in (2.29). We construct the solution associated with the jth term by setting $\hat{Q} = a_j \exp\left[-\left(\dfrac{x}{r}\right)^2\right]$ and $m = j\Delta m$, solving (2.16-2.17) using the same differencing methods as before, and then substituting into (2.18-2.21) (replacing m_0 with m).

Below 3 km the temperature, pressure and wind fields are similar to those in the previous simulation both in structure and magnitude (Figure 2.6(a-c)). The vertical-motion field has a similar pattern, but is much less intense (Figure 2.6(d)). Between 3 and 4 km all fields differ from those in the previous simulation. The perturbation temperature becomes positive near 4 km, and pressure and wind perturbations have the same sign but are much weaker. Above 4 km anomalies in all fields radiate up and away from the forcing.

Our method of solving (2.1-2.4) provides a physical interpretation of the similarities and differences between the two simulations. In the first simulation the forcing excites a single vertical mode in the form of two buoyancy waves. In the second simulation the forcing excites a continuum of vertical modes, and each comprises two buoyancy waves. The phase speed of the buoyancy-wave pair is inversely proportional to the wave number of the mode, so the wave pairs disperse. Those modes whose vertical wave number is close to that of the heating ($j \approx 10$, Figure 2.5, top) are excited the most and their net contribution to the atmospheric response resembles a horizontally-smoothed version of the single-mode response in the first simulation. This smoothing most strongly modifies the vertical motion field because its features have the smallest horizontal scale.

Pandya et al. (1993) provided an analytical solution to (2.1-2.4) for a thermal forcing that was 10 km deep and entirely positive. Their solution for the unbounded atmosphere compared less favorably to the corresponding solution for the bounded atmosphere (Nicholls et al. 1991). To understand this difference we consider the ratio of the horizontal scale of the response to that of the forcing for the two sets of simulations. For the simulations conducted by Pandya et al. (1993) and Nicholls et al. (1991) the forcing had a radius of 10 km, and after two hours of forcing the response had a radius of about 240 km, so this ratio was about 24. For the simulations presented here after four hours the ratio is about 4. This ratio provides a relative estimate of the dispersion of the vertical modes which comprise the solution for the unbounded atmosphere. Thus for the simulation presented here there was about one-sixth as much dispersion, and much less distortion of the bounded solution. We conclude that as long as the ratio of scales is sufficiently small, using a rigid upper-boundary allows for simple, somewhat realistic simulations of the atmospheric response to convection.

2.4 The Coriolis force

A third limitation of the dynamical system is that it neglects the Coriolis force. In this section we examine how including this force alters the preliminary simulation.

The rotational version of (2.1-2.4) is as follows:

$$\frac{\partial u}{\partial t} - fv + \frac{1}{\rho_0}\frac{\partial p}{\partial x} = 0 \tag{2.31}$$

$$\frac{\partial v}{\partial t} + fu = 0 \tag{2.32}$$

$$\frac{1}{\rho_0}\frac{\partial p}{\partial z} = b \tag{2.33}$$

$$\frac{\partial b}{\partial t} + wN^2 = Q \tag{2.34}$$

$$\frac{\partial u}{\partial x} + \frac{\partial w}{\partial z} = 0 \tag{2.35}$$

where v denotes velocity in the y-direction, f ($9.35\ x\ 10^{-5}\ s^{-1}$) is the Coriolis parameter and the other variables are as before. We solve (2.31-2.35) by reducing the system to the rotational non-dimensional shallow water equations and then solving them using the same differencing methods as before, except here we set $[x] = \dfrac{N}{m_0 f}$ or 136 km (one Rossby radius), $\Delta x' = 0.05$ and $\Delta t' = 0.025$.

After two hours of forcing the fields of perturbation temperature, pressure and zonal wind are nearly identical to those in the preliminary simulation (Figure 2.7(a-c)). At four hours there are some differences--the buoyancy waves are slightly less intense, and perturbations in temperature and pressure remain in the vicinity of the forcing. These differences may be understood in terms of geostrophic adjustment theory (e.g. Holton 1992). Within the irrotational system the forcing excites only buoyancy waves, but within the rotational system there are both buoyancy waves and a balanced response. Since the radius of the forcing is about half of a Rossby radius, and its duration is only two-thirds of an inertial period, the balanced response is weaker than the buoyancy-wave response. At four hours the balanced and buoyancy-wave responses are superposed, but by six hours they separate, so that the structure of the balanced response is more salient (Figure 2.7(a, b,d)). It includes a surface high where the forcing was, northerlies to the east of the high and southerlies to the west of the high.

Although the balanced response contributes noticeably to the surface-pressure field, we neglect it for the remainder of this paper in order to focus on the buoyancy-wave response. For a more detailed discussion of the balanced response excited by squall systems the reader is referred to Hertenstein and Schubert (1991).

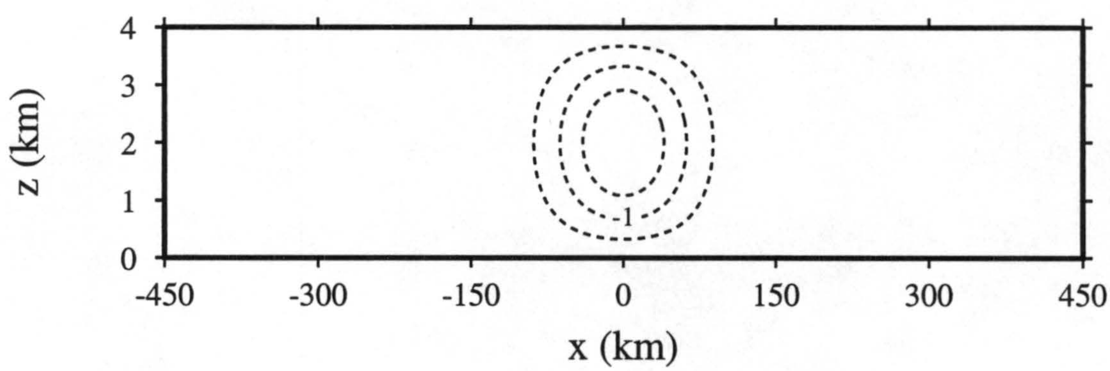

Figure 2.1. The thermal forcing for $t \leq 2$ h. The units have been converted to K h^{-1} by multiplying by $\frac{T}{g}$ where $T = 273$ K. The contour interval is 0.5 K h^{-1}.

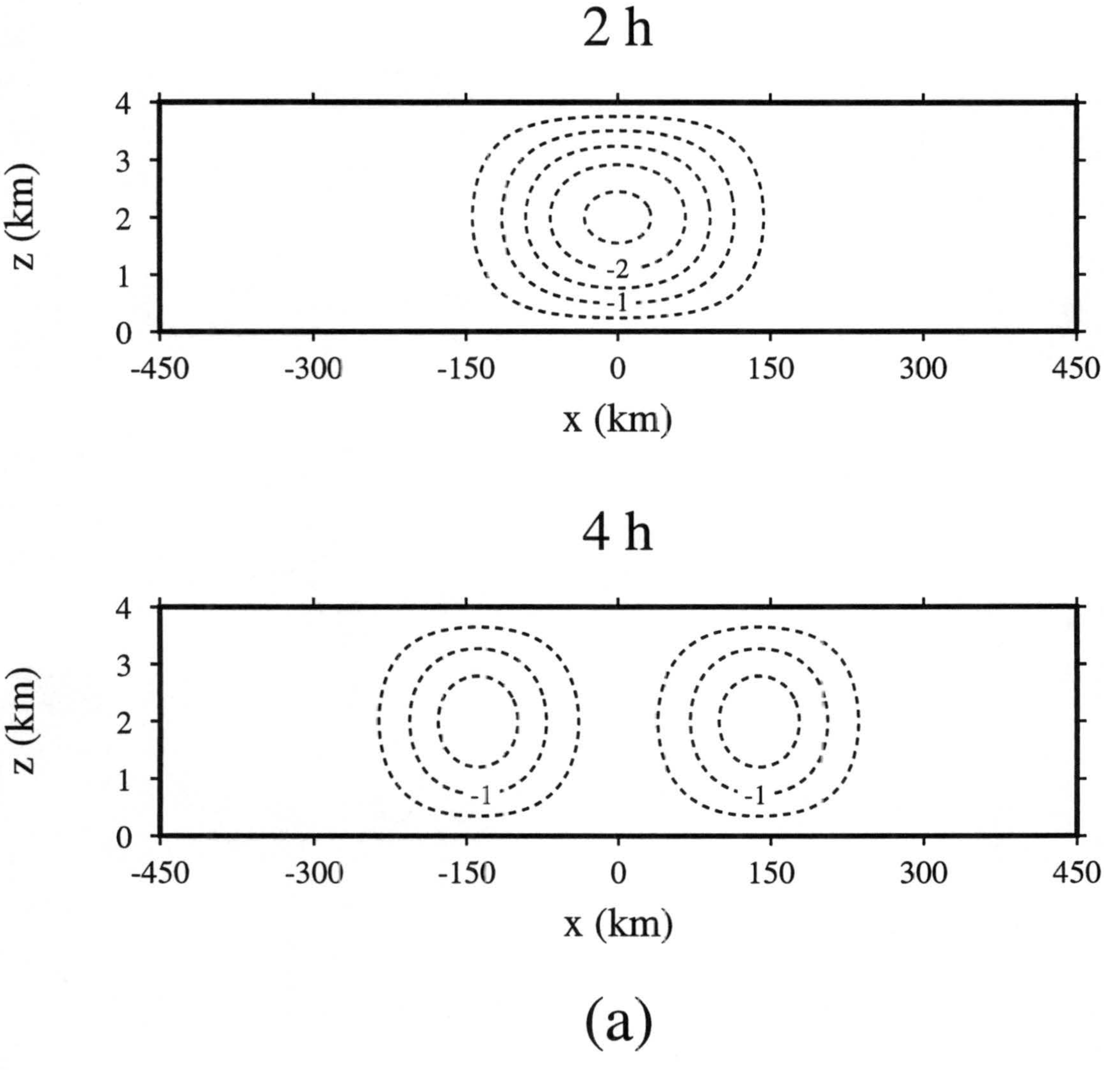

Figure 2.2. The atmospheric response to the thermal forcing. (a) perturbation temperature with a 0.5 K contour interval. Perturbation temperature was calculated by multiplying perturbation buoyancy by $\frac{T}{g}$ where $T = 273$ K.

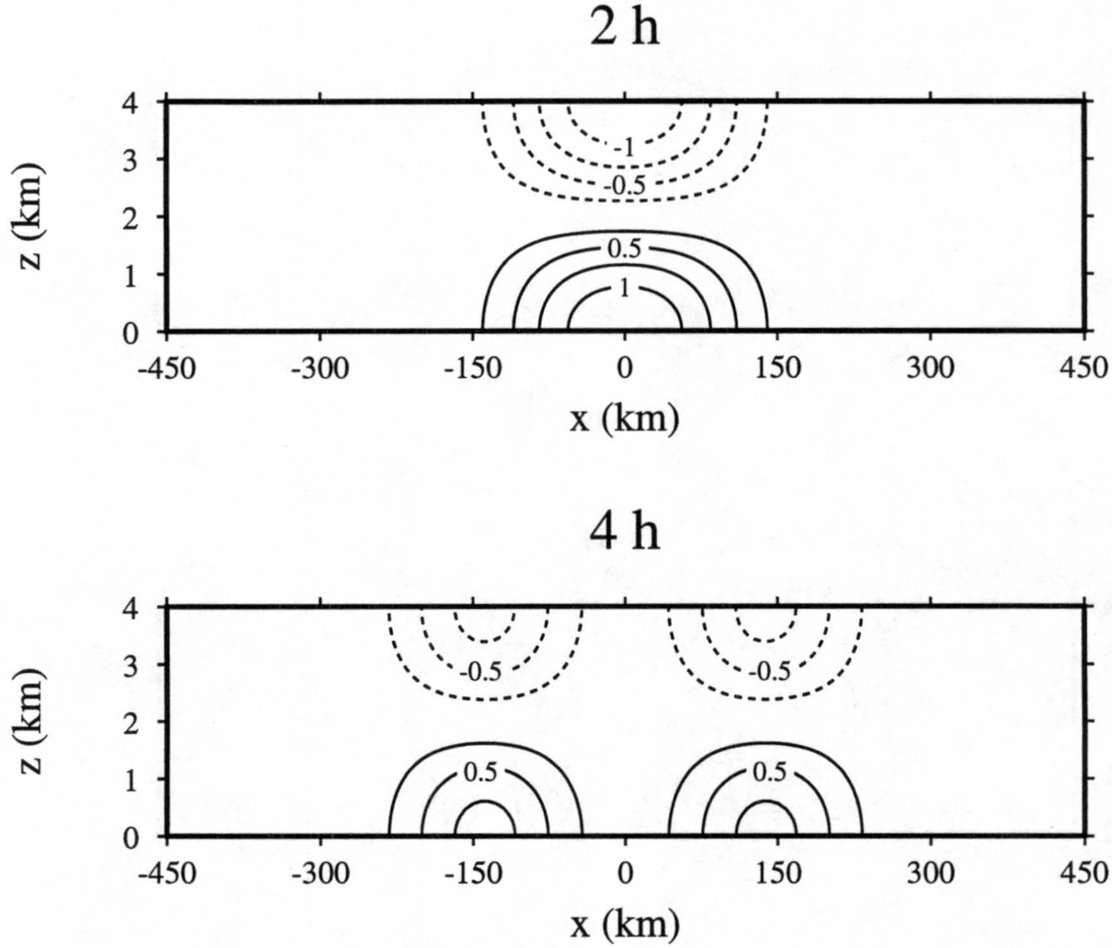

(b)

Figure 2.2 (continued). (b) perturbation pressure with a 0.25 hPa contour interval. The zero contour is omitted.

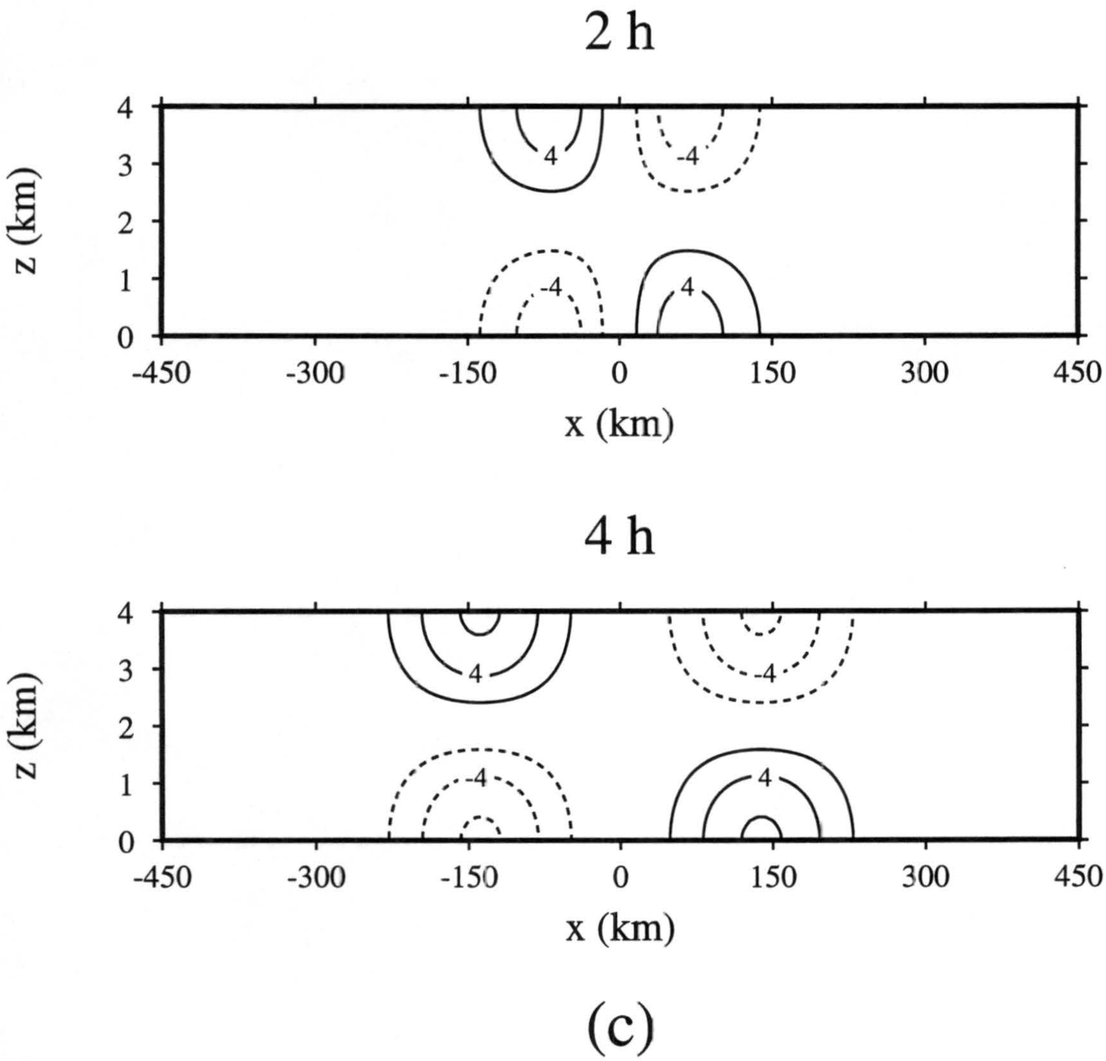

Figure 2.2 (continued). (c) perturbation wind with a 2 m s^{-1} contour interval. The zero contour is omitted.

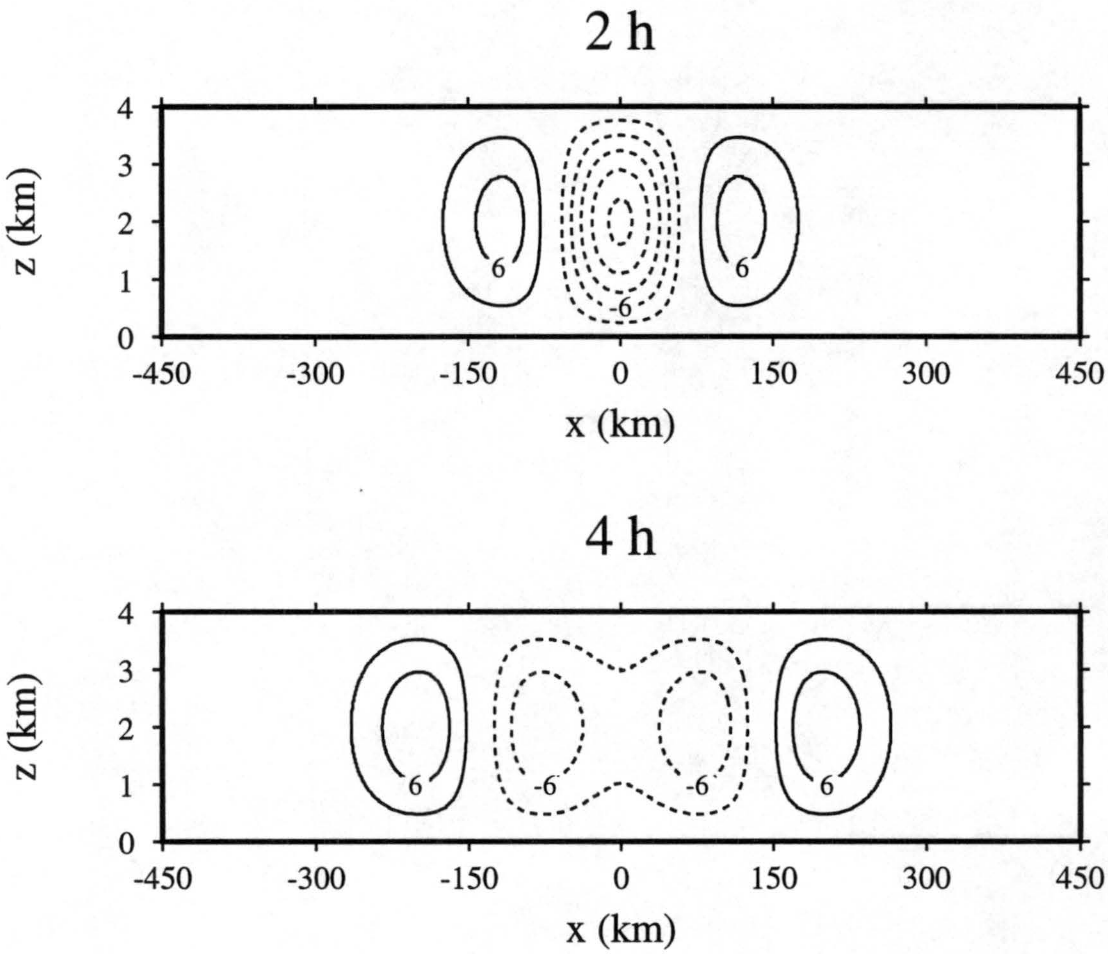

(d)

Figure 2.2 (continued). (d) vertical motion with a 3 cm s^{-1} contour interval. The zero contour is omitted.

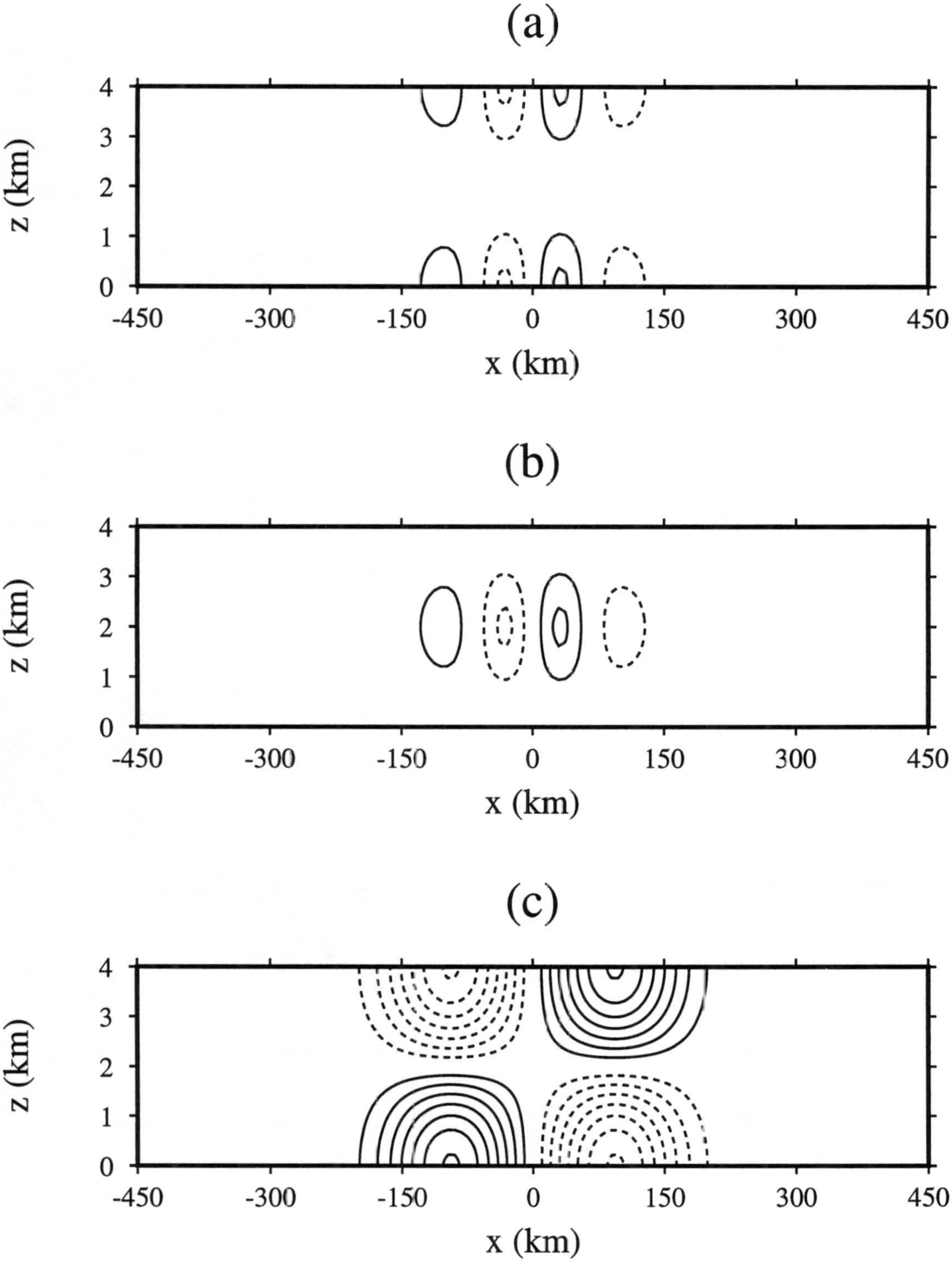

Figure 2.3. (a) $u\,\dfrac{\partial u}{\partial x}$, (b) $w\,\dfrac{\partial u}{\partial z}$, and (c) $\dfrac{1}{\rho_0}\,\dfrac{\partial p}{\partial x}$ at 2 h. The contour interval is 0.5 m s^{-1} h^{-1}, the positive contours are solid, the negative contours are dashed, and the zero contours are omitted.

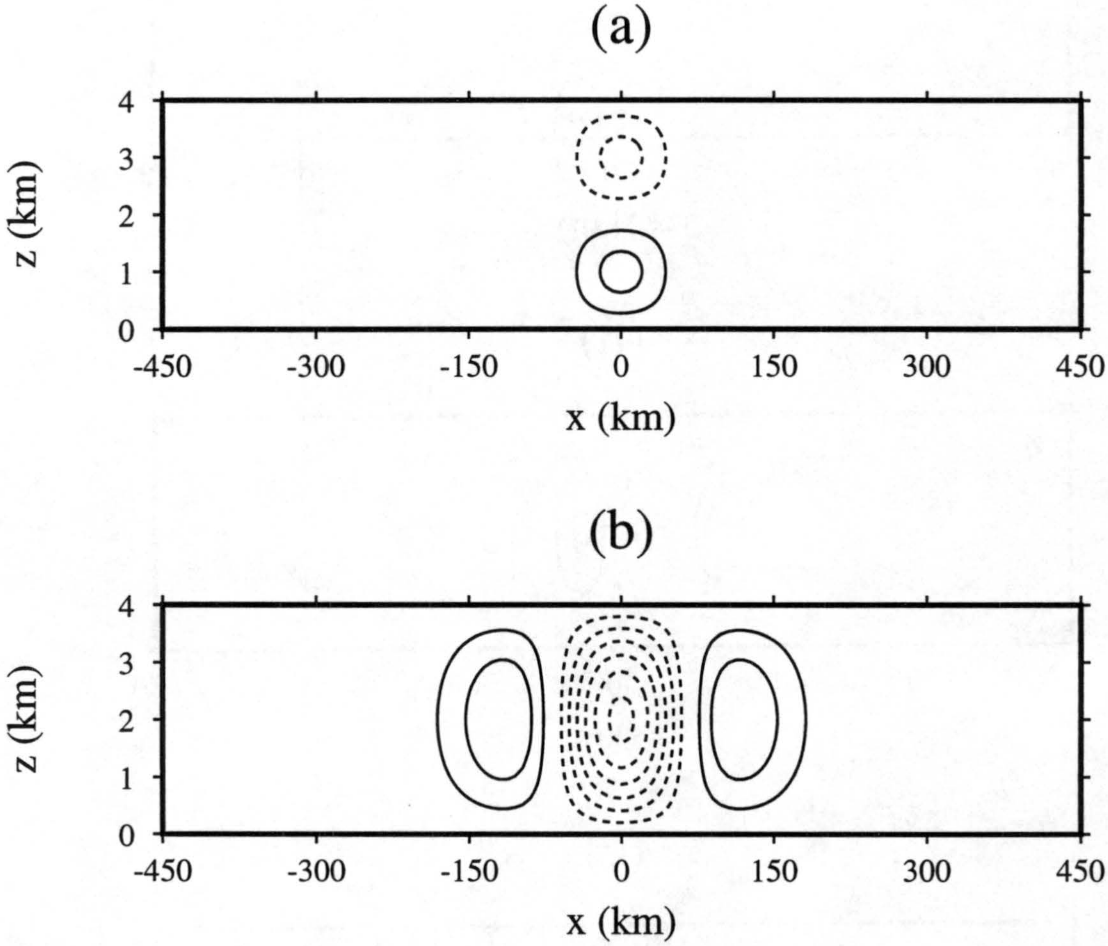

Figure 2.4. (a) $w\dfrac{\partial b}{\partial z}(\dfrac{T}{g})$ and (b) $wN^2(\dfrac{T}{g})$ at 2 h. The contour interval is 0.25 K h^{-1}, the positive contours are solid, the negative contours are dashed, and the zero contours are omitted.

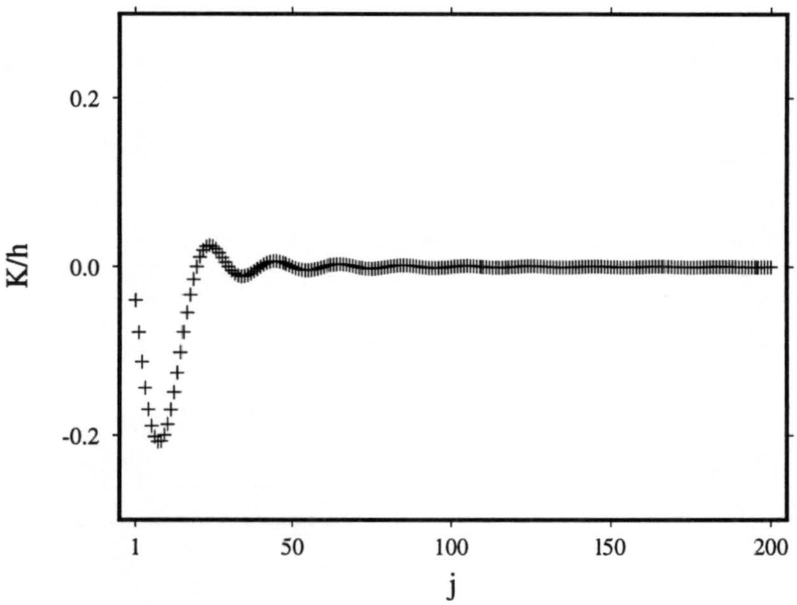

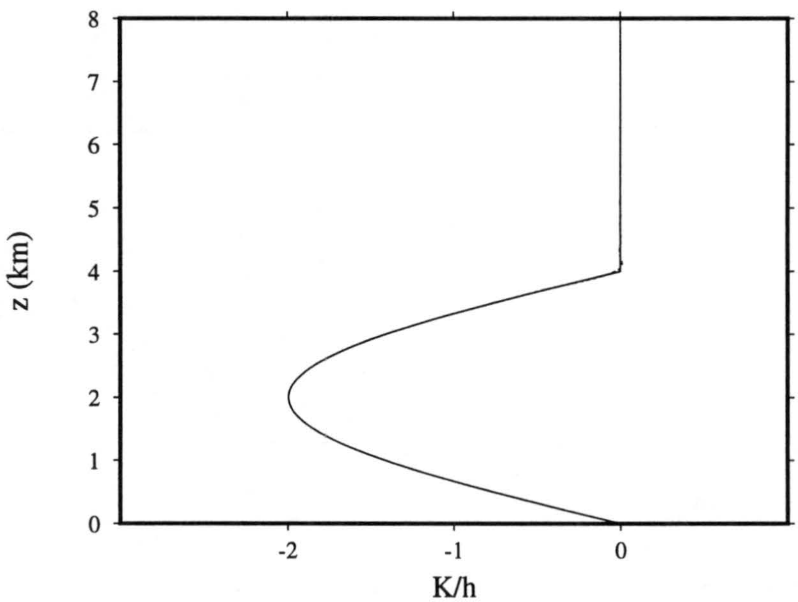

Figure 2.5. The values of a_j used in the simulation for the unbounded atmosphere (top). A comparison between the exact function $\tilde{Q}$ (solid) and the approximation of $\tilde{Q}$ (dashed) given by (2.29) (bottom). For both plots the units have been converted to K h^{-1} by multiplying by $\dfrac{T}{g}$ where $T = 273$ K.

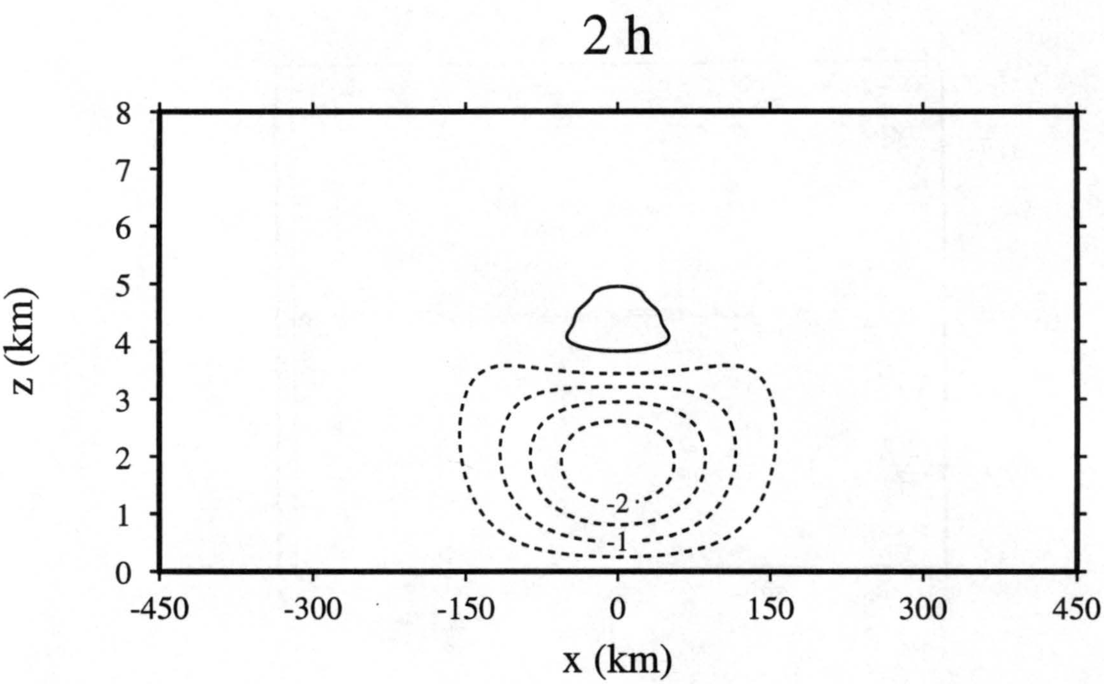

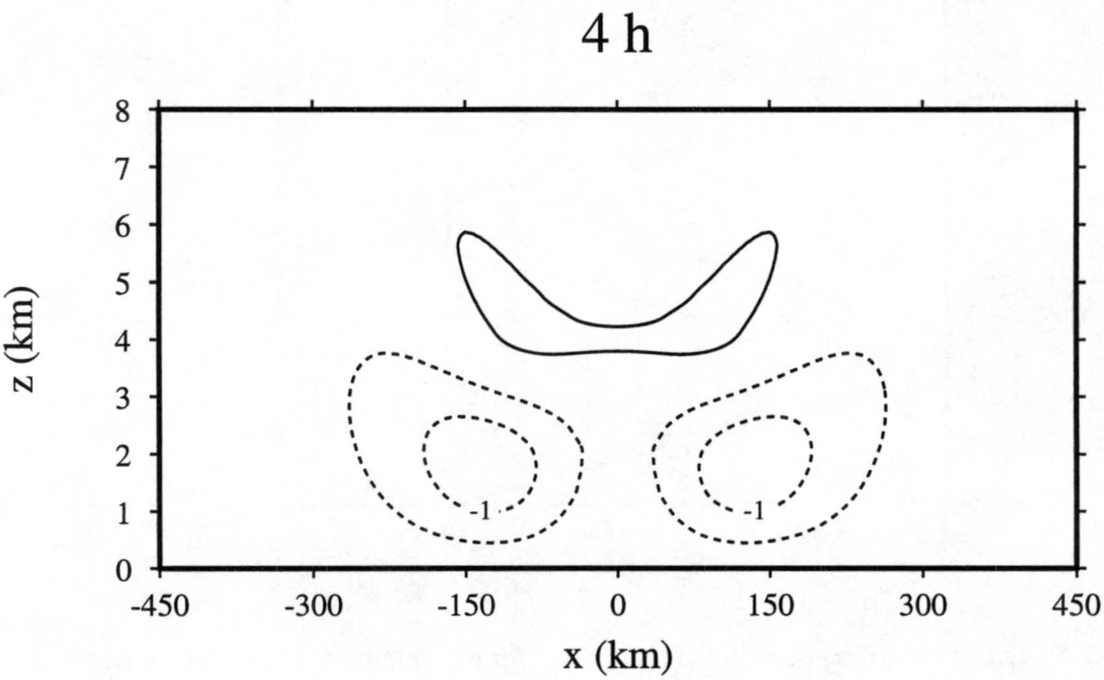

(a)

Figure 2.6. The response of the unbounded atmosphere to the thermal forcing. (a) perturbation temperature contoured as in Figure 2.2.

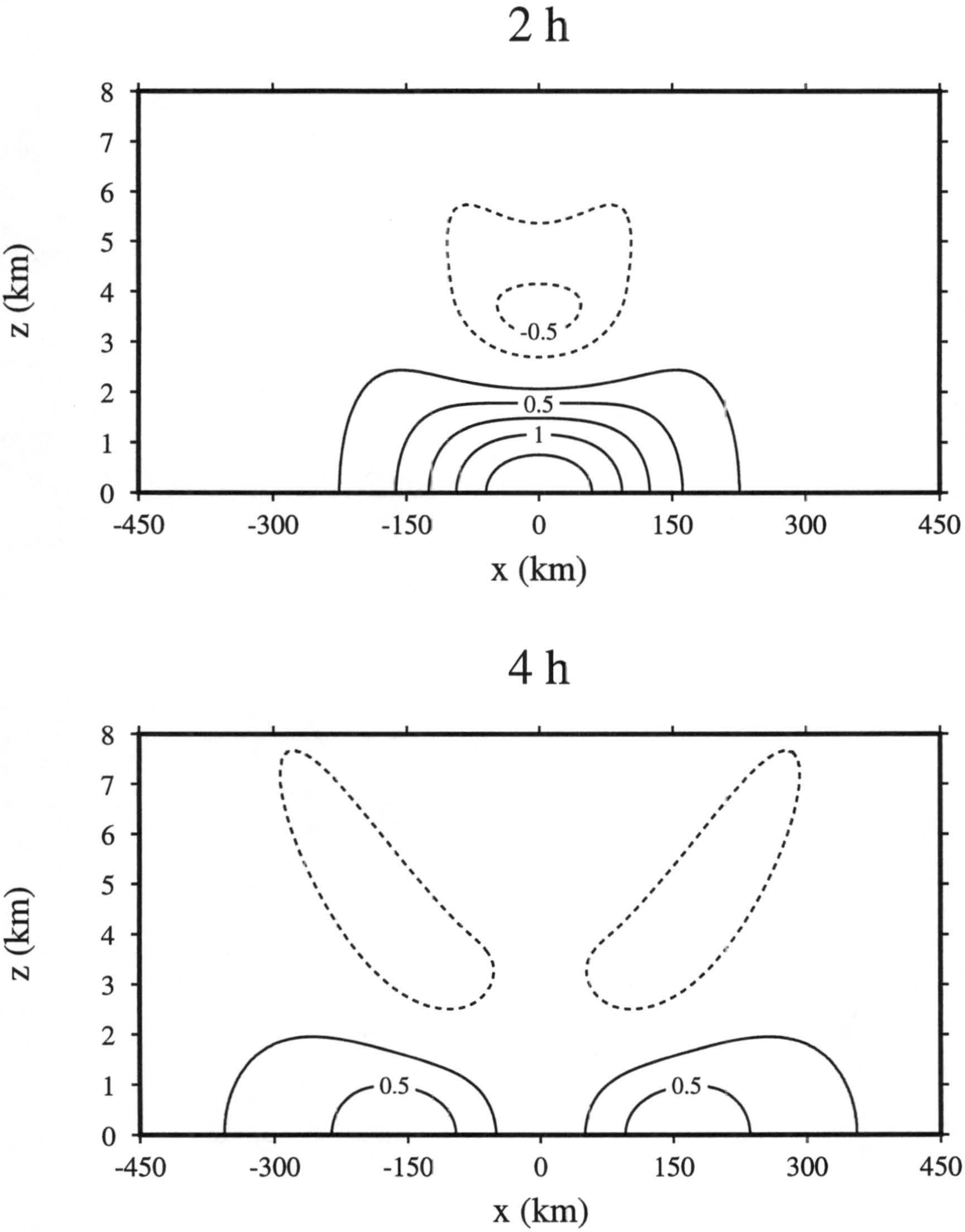

(b)

Figure 2.6 (continued). (b) perturbation pressure contoured as in Figure 2.2.

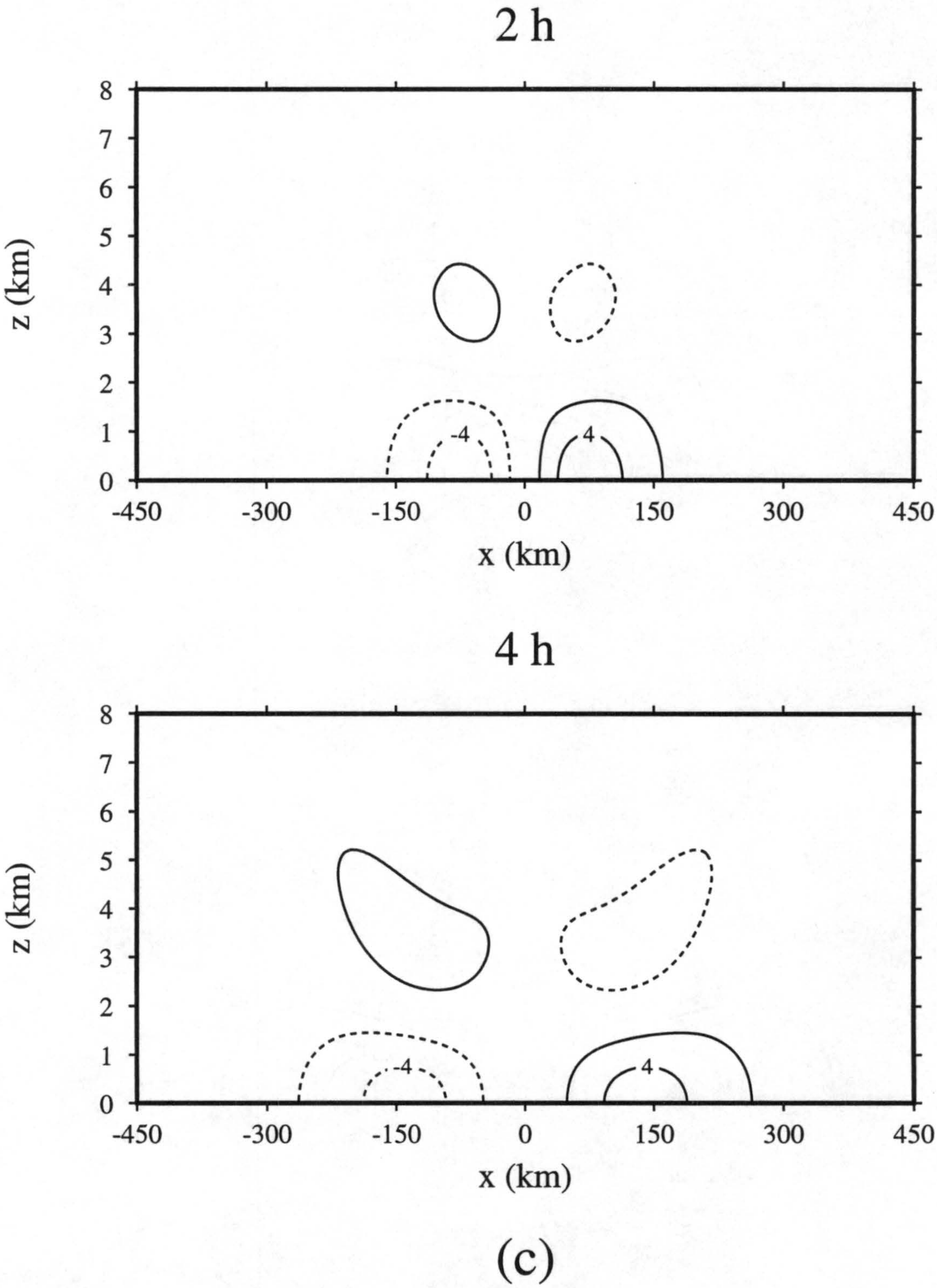

Figure 2.6 (continued). (c) perturbation wind contoured as in Figure 2.2.

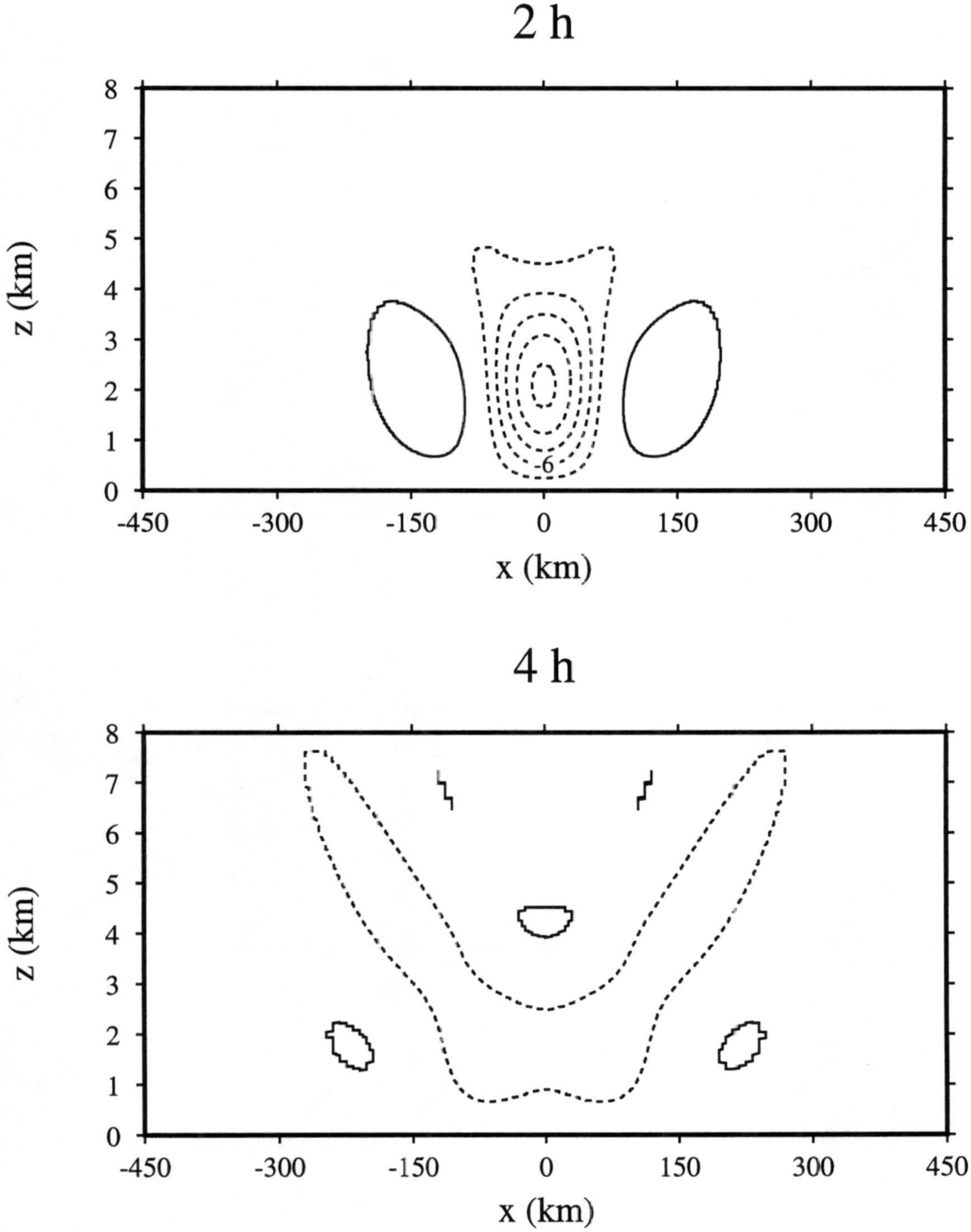

(d)

Figure 2.6 (continued). (d) vertical motion contoured as in Figure 2.2.

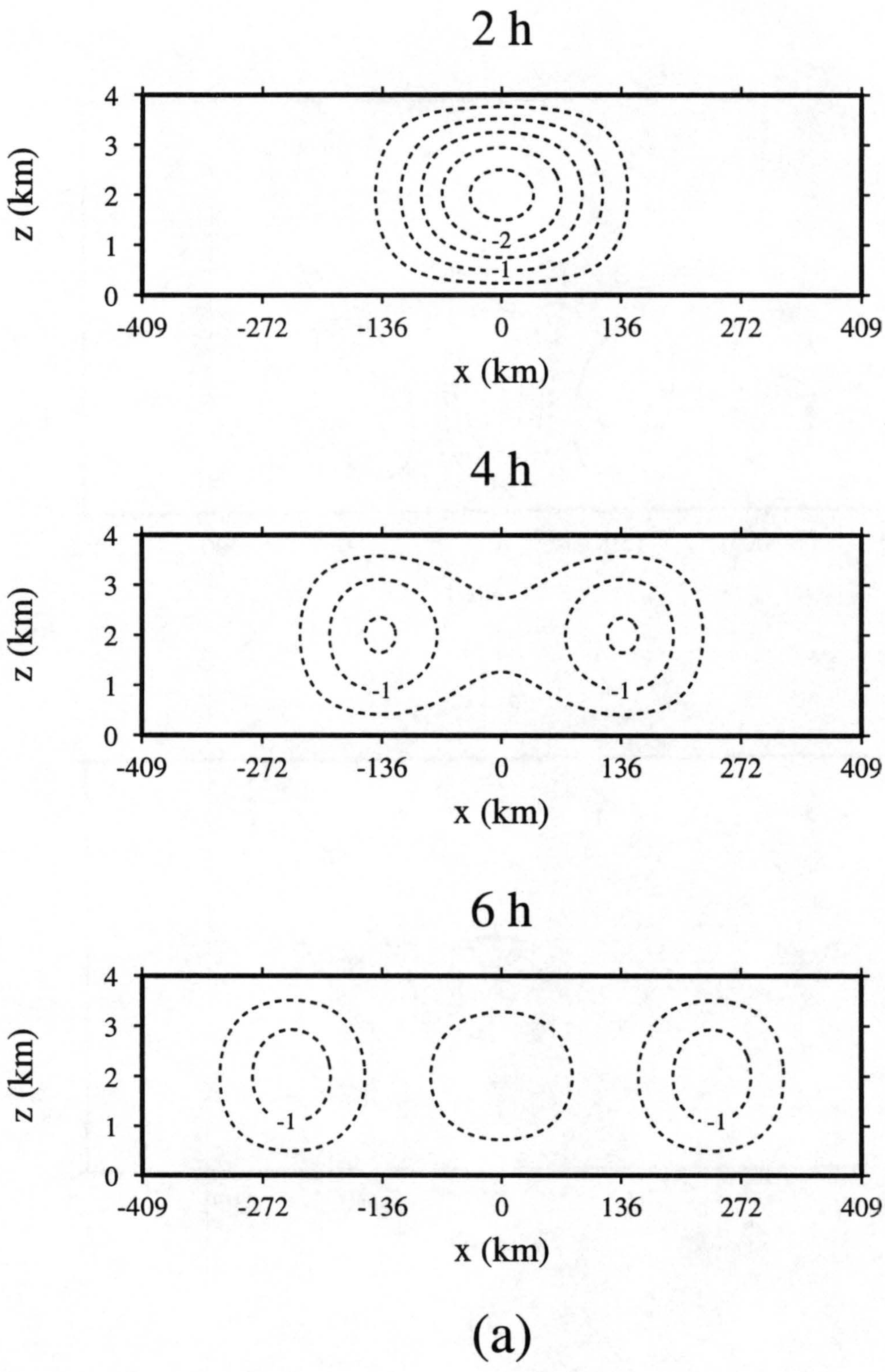

Figure 2.7. The response of the rotational atmosphere to the thermal forcing. (a) perturbation temperature contoured as in Figure 2.2.

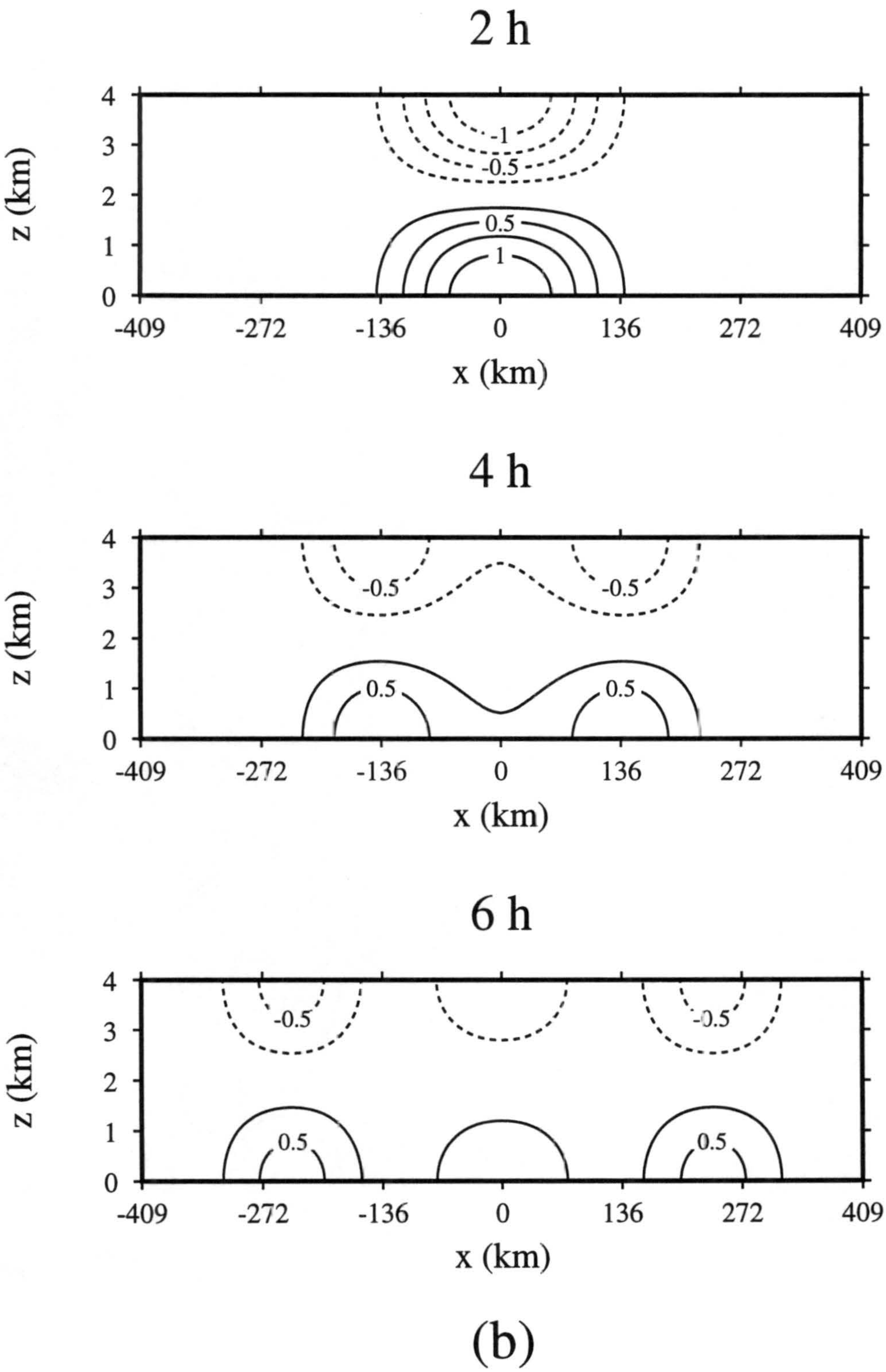

(b)

Figure 2.7 (continued). (b) perturbation pressure contoured as in Figure 2.2.

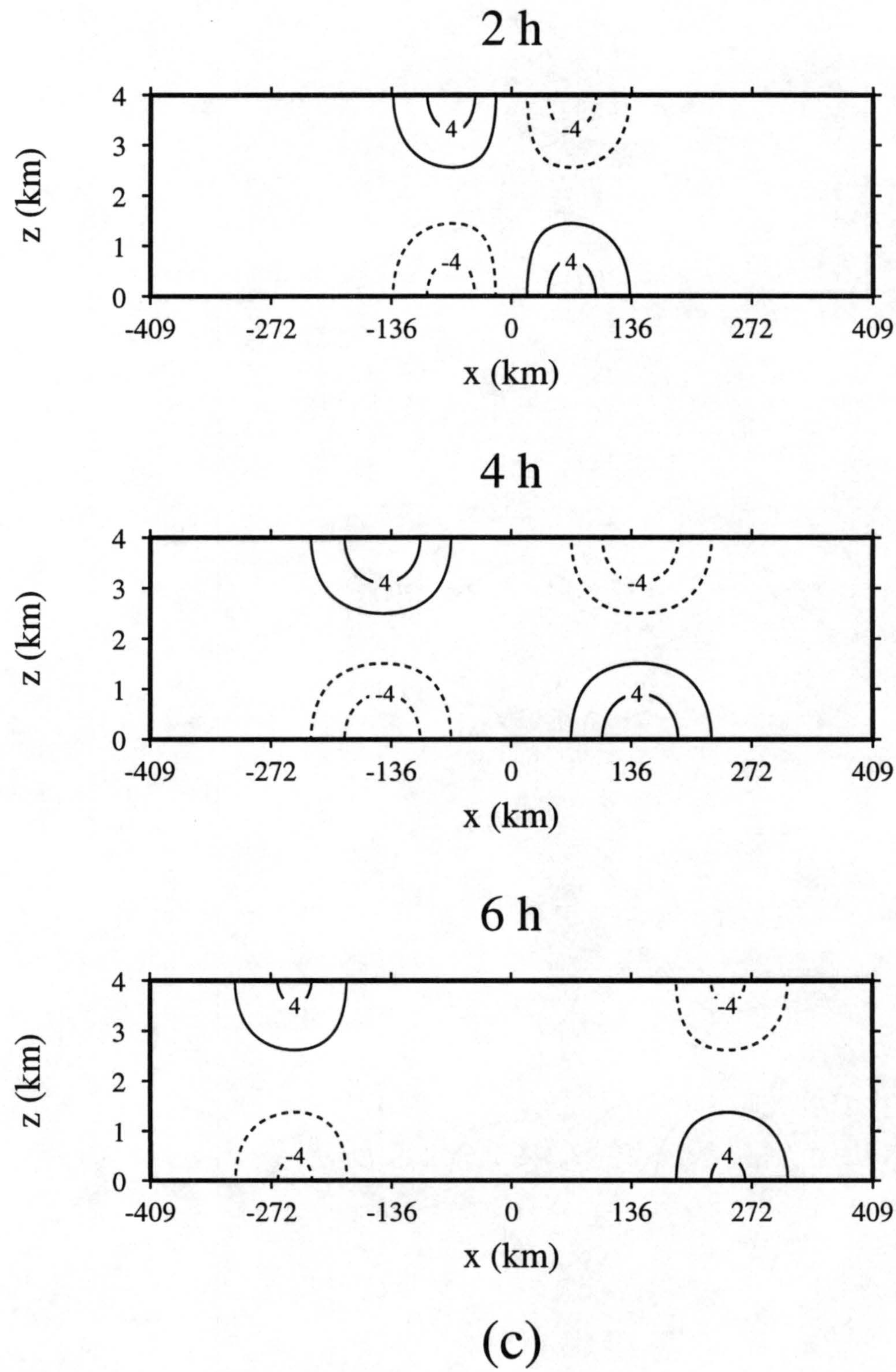

Figure 2.7 (continued). (c) perturbation zonal wind contoured as in Figure 2.2.

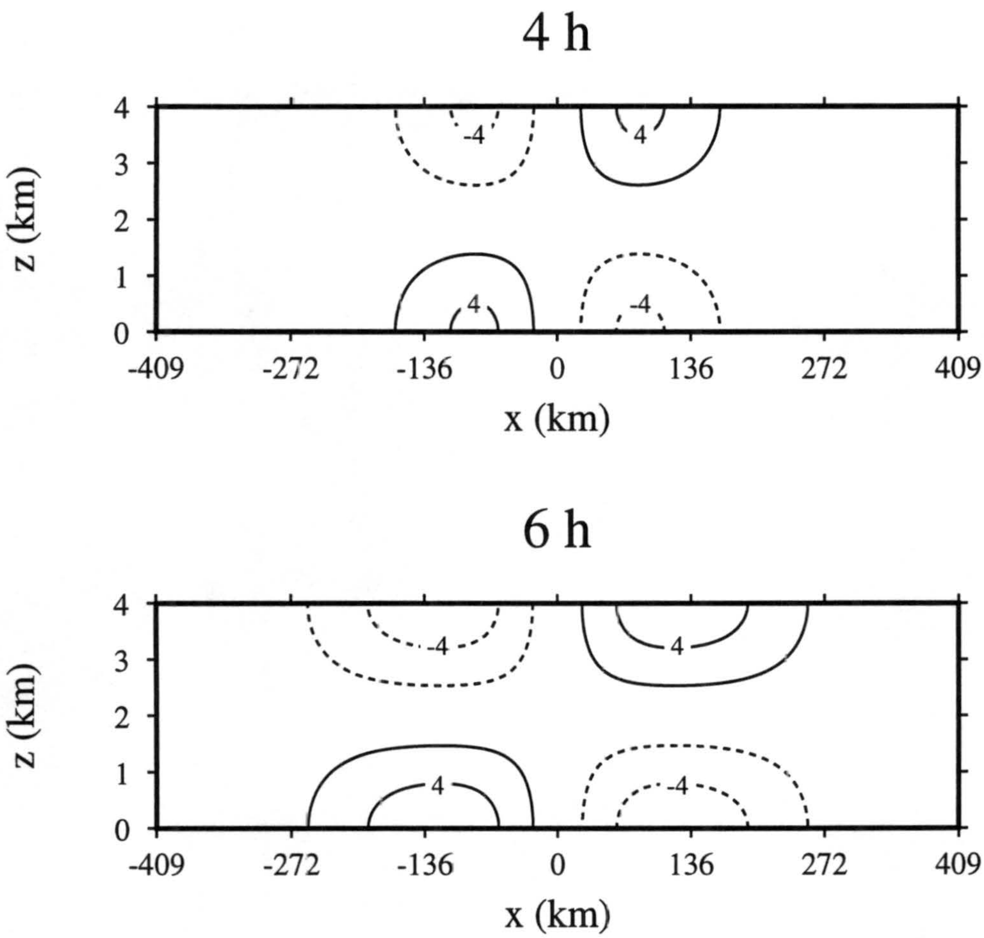

(d)

Figure 2.7 (continued). (d) perturbation meridional wind with a 2 m s^{-1} contour interval. The zero contour is omitted.

Chapter 3

SIMULATIONS OF MESOHIGHS AND WAKE LOWS

This chapter contains several simulations of the lower-tropospheric circulation and the surface-pressure features within mesoscale convective systems. For each simulation the only forcing is the low-level cooling associated with stratiform precipitation. The simulations show that the buoyancy-wave response to this forcing closely resembles observations of mesohighs and wake lows. This response is sensitive to both the movement of the forcing and its three-dimensional nature.

3.1 Moving, two-dimensional forcing

In Chapter 2 we simulated the atmospheric response to the low-level cooling associated with a stationary, two-dimensional stratiform region. In this section we examine how this response changes when the stratiform region moves. We define the forcing as follows:

$$Q(x,z,t) = Q_0\, Q_x(x-ct)\, \sin(m_0 z) \tag{3.1}$$

where Q_0, Q_x and m_0 are as before and c = 10 m s^{-1}. This value of c is somewhat arbitrary. Some stratiform regions move at about this speed with respect to the low-level flow; others moves faster, and still others are nearly stationary. The sensitivity of the response to the magnitude of c is discussed in the next chapter. We solve (2.1-2.4) for this forcing as we did in section 2.1.

Just as in the preliminary simulation the forcing generates two buoyancy waves, one which propagates eastward and one which propagates westward (Figure 3.1). Since the forcing never shuts off, the horizontal scale of each wave grows with time. The wave front associated with the eastward-propagating wave separates from the center of the forcing more slowly, so this wave grows in scale more slowly. The forcing contributes equal cooling to each of the two waves so that the eastward-propagating wave becomes much more intense. Within this wave perturbation surface pressure reaches a maximum of nearly 3 hPa (Figure 3.1(b)), the minimum perturbation temperature falls below -6 K (Figure 3.1(a)) and surface westerlies reach 19 m s^{-1} (Figure 3.1(c)). On the leading edge of the wave there is rising motion which peaks at 27 cm s^{-1}, and on the trailing edge of the wave there is subsidence with a maximum intensity of 33 m s^{-1} (Figure 3.1(d)). The buoyancy, horizontal-wind and vertical-velocity fields have the same structure as those in a numerical simulation of squall-system low-level cooling carried out by Lin and Smith (1986).

An apparent buoyancy wave similar to the eastward-propagating wave generated in the simulation occurred in a squall-system over the central United States on 3-4 June 1985 (Stumpf et al. 1991). A line-perpendicular cross-section of radar reflectivity through the western part of the stratiform region is shown in Figure 3.2. The precipitation has a distinct western boundary at -68 km. Surface pressure falls rapidly across this boundary near a region of lower tropospheric subsidence. Within the simulation there is a similar surface-pressure fall across the western edge of the forcing which is also accompanied by lower-tropospheric subsidence (Figure 3.1(b,d)). We do not directly compare the observed winds to the simulated winds, because the simulation occurred in a basic state of rest, and the 3-4 June squall system occurred in an an environment with considerable shear. However, we do note that the horizontal variation of the observed winds is similar to that in the simulation. Near the surface the winds are more westerly (less easterly) within the stratiform region than they are to its west, and near a height of 4 km the winds are more easterly in the stratiform region than they are to its west.

Not only do the surface-pressure, horizontal-wind and vertical-velocity fields observed in the 3-4 June squall system resemble those in the simulation, but so does the observed perturbation temperature field. Figure 3.3, which has the same domain as Figure 3.2, shows a dynamic retrieval (Hane and Ray 1985) of perturbation temperature for the squall system. The largest and most intense feature of this field is a cool anomaly between 1.5 and 4.5 km which exists throughout the stratiform region. The subsidence occurs on the western edge of this anomaly (Figure 3.2) just as it does in the simulation (Figure 3.1(a,d)).

Since the numerical simulation appears to be fairly realistic, we can use it to address the unanswered questions presented in Chapter 1, namely why is the maximum surface pressure found ahead of the maximum in low-level cooling, and what causes the subsidence at the western edge of the stratiform region? To answer the first question we consider the source of the cool anomaly that developed after six hours at $x = 240$ km, $z = 2$ km (Figure 3.1(a)). Within the dynamical system local changes in buoyancy (or temperature) are caused by vertical motion and/or direct forcing. We can quantify the contribution of each by integrating Equation (2.3) with respect to time:

$$b(x,z,t) = b(x,z,0) - N^2 \int_0^t w \, d\tilde{t} + \int_0^t Q \, d\tilde{t} \qquad (3.2)$$

where $\tilde{t}$ is a dummy variable. We have performed this integration for the cool anomaly in question, and vertical motion accounts for 61 percent of it. This vertical motion occurred on the leading edge of the buoyancy wave. It occurred ahead of the forcing because the buoyancy-wave phase speed (13 m s^{-1}) is greater than the speed of the forcing (10 m s^{-1}). It seems surprising that vertical motion, which may be the single most important factor for causing the mesohigh, is often not even mentioned as a source of the coolness of the lower-troposphere above the mesohigh.

The simulation also provides information about the cause of the subsidence responsible for the wake low. Within the dynamical system vertical motion is a diagnostic variable which depends on the horizontal flow according to the continuity equation. Thus, asking what causes the subsidence on the trailing edge of the forcing is equivalent to asking what causes the low-level divergence and the mid-level convergence there. In the vicinity of the subsidence the pressure gradient at low-levels is decelerating the westerlies, and the pressure gradient at mid-levels is decelerating the easterlies. Where the low-level westerlies are decelerating there is lower-level divergence, and where the mid-level easterlies are decelerating there is upper-level convergence. In a sentence, the subsidence is the trailing portion of the buoyancy-wave circulation.

Although the simulation provides remarkable insight considering its simplicity, it has several limitations. First, late in the simulation the magitude of the perturbation wind and the gradients in all fields are significantly greater than they are in the preliminary simulation, and so are the relative magnitudes of nonlinear terms. A nonlinear simulation might be significantly different by six hours. Second, the subsidence observed in the 3-4 June squall system was much more intense and more localized than it is in the simulation. This difference may be related to the exclusion of the nonlinear terms or the horizontal scale of the forcing. Third, within the simulation the perturbation surface pressure never becomes negative, as it apparently did in regions of the 3-4 June squall system and many other systems. This limitation seems to be related to the dynamical system's lack of a third dimension, and it is discussed in the next section.

3.2 Stationary, three-dimensional forcing

The three-dimensional version of our dynamical system is as follows:

$$\frac{\partial u}{\partial t} + \frac{1}{\rho_0}\frac{\partial p}{\partial x} = 0 \tag{3.3}$$

$$\frac{\partial v}{\partial t} + \frac{1}{\rho_0}\frac{\partial p}{\partial y} = 0 \tag{3.4}$$

$$\frac{1}{\rho_0}\frac{\partial p}{\partial z} = b \tag{3.5}$$

$$\frac{\partial b}{\partial t} + wN^2 = Q \tag{3.6}$$

$$\frac{\partial u}{\partial x} + \frac{\partial v}{\partial y} + \frac{\partial w}{\partial z} = 0 \tag{3.7}$$

where v is velocity in the y-direction, and the other variables are as before. For this section we define the thermal forcing to be stationary, transient and Gaussian in both x and y:

$$Q(x, y, z, t) = Q_0\, Q_{xy}(x, y)\, \sin(m_0 z)\, Q_t(t) \tag{3.8}$$

where Q_0, m_0 and Q_t are as before and $Q_{xy} = \exp\left[\frac{-x^2 - y^2}{r^2}\right]$ where $r = 100$ km. We solve (3.3-3.7) for this forcing using the procedure discussed in section 2.1. The only difference is that here the system reduces to the *two-dimensional,* irrotational shallow water equations.

Both the forcing and its response are axisymmetric, so it would be natural to view the response using plots with radius as one axis and height as the other. However, we wish to compare the response to those of previous and following simulations, and vertical (Figure 3.4) and horizontal (Figure 3.5) cross sections better serve that purpose. The forcing generates a cool anomaly and an accompanying surface mesohigh with a maximum amplitude of 1.1 hPa by 2 hours (Figures 3.4(a-b) and 3.5(a)). Just as in the preliminary simulation there is mid-level convergence, low-level divergence and subsidence above the mesohigh (Figure 3.4(c-d)). There is also rising motion in a ring around the mesohigh, but it is much weaker than the subsidence. The rising motion covers a greater horizontal area, however, so that the average vertical motion over the entire region is zero. After the forcing ends the surface pressure falls rapidly in the vicinity of the mesohigh (Figures 3.4(b) and 3.5(b)), but unlike the preliminary simulation the surface pressure becomes negative. In both simulations the surface-pressure fall results from lower-tropospheric warming (Figure 3.4(a)) associated with subsidence. The subsidence is driven by the inertia of the horizontal flow, and it is more intense in this case because the mid-level flow above the mesohigh converges in two dimensions, and the low-level flow below it diverges in two dimensions. By five hours the pressure is already begining to rise again--there is weak rising motion and adiabatic cooling above the mesolow (Figure 3.4(d)).

This simulation resembles a portion of the lifetime of a squall system observed over the central United States on 23-24 June 1985 (Johnson et al. 1989). At about 05 UTC on June 24 a region of stratiform precipitation developed over southwestern Kansas and northwestern Oklahoma. It lasted for several hours, moving little, and then rapidly dissipated (Figure 3.6). A large and intense mesohigh with strongly divergent surface winds developed beneath the precipitation. After the precipitation ended a short-lived wake low developed where the mesohigh had been. Soundings taken in the vicinity of the mesohigh and mesolow showed that this pressure fall was a consequence of lower-tropospheric warming, probably caused by subsidence (Figure 3.7).

3.3 Moving, three-dimensional forcing

In this section we define the thermal forcing to resemble the stratiform cooling of a classical squall system. It has the same spatial dependence as the forcing in the previous section, it moves at 10 m s^{-1}, and it lasts for six hours:

$$Q(x, y, z, t) = Q_0 \, Q_{xy}(x - ct, y) \sin(m_0 z) \, Q_t \tag{3.9}$$

where Q_0, Q_{xy}, c and m_0 are as before and $Q_t = 1$ for $t \leq 6$ h and $Q_t = 0$ for $t > 6$ h.

After two hours of forcing a surface mesohigh with a maximum pressure of 1.1 hPa has developed beneath the forcing (Figure 3.8(a)). The high moves eastward and intensifies to 1.4 hPa by 4 hours (Figure 3.8(b)). By this time the location of the maximum surface pressure has shifted ahead of the center of the forcing, just as it did in the simulation presented in Section 3.1. A weak wake low has also developed, and it trails the center of the forcing by about 150 km. By six hours the maximum surface pressure surpasses 1.5 hPa, and the minimum pressure becomes negative in the center of the wake low (Figure 3.8(c)). Since the forcing does not end until exactly this time, we cannot attribute this negative pressure to the dissipation of the forcing. Rather it is entirely a consequence of the motion of the forcing. After the forcing ends there is a significant pressure fall in its vicinity, just as there was in the simulation presented in Section 3.2. The wake low intensifies to -0.9 hPa and the mesohigh weakens (Figure 3.8(d)).

The life cycle of the surface-pressure features shown in Figure 3.8 resembles the one which Fujita (1955) identified (Figure 1.2). In both cases at first there is only a mesohigh. It intensifies and then a wake low forms and intensifies as the mesohigh dissipates. The wake low reaches its maximum intensity after the forcing has dissipated. The mature structure of the simulated mesohigh and wake low (Figure 3.8(c)) also resembles the schemata constructed by Johnson and Hamilton (1988) (Figure 1.1) and Loehrer and Johnson (1995) (Figure 1.3). The mesohigh lies ahead of the stratiform forcing, and the wake low trails the stratiform forcing. There are perturbation westerlies within the mesohigh and perturbation easterlies within the wake low.

Within this chapter we have seen that buoyancy-wave responses to stratiform coolings closely resemble observations of MCS mesohighs and wake lows. We have found that a moving forcing generates a more intense response than a stationary forcing, that a forcing must be three-dimesional in order for it to generate a negative perturbation in surface-pressure, and that a classical squall-system stratiform cooling generates mesohighs and wake lows with a realistic life cycle.

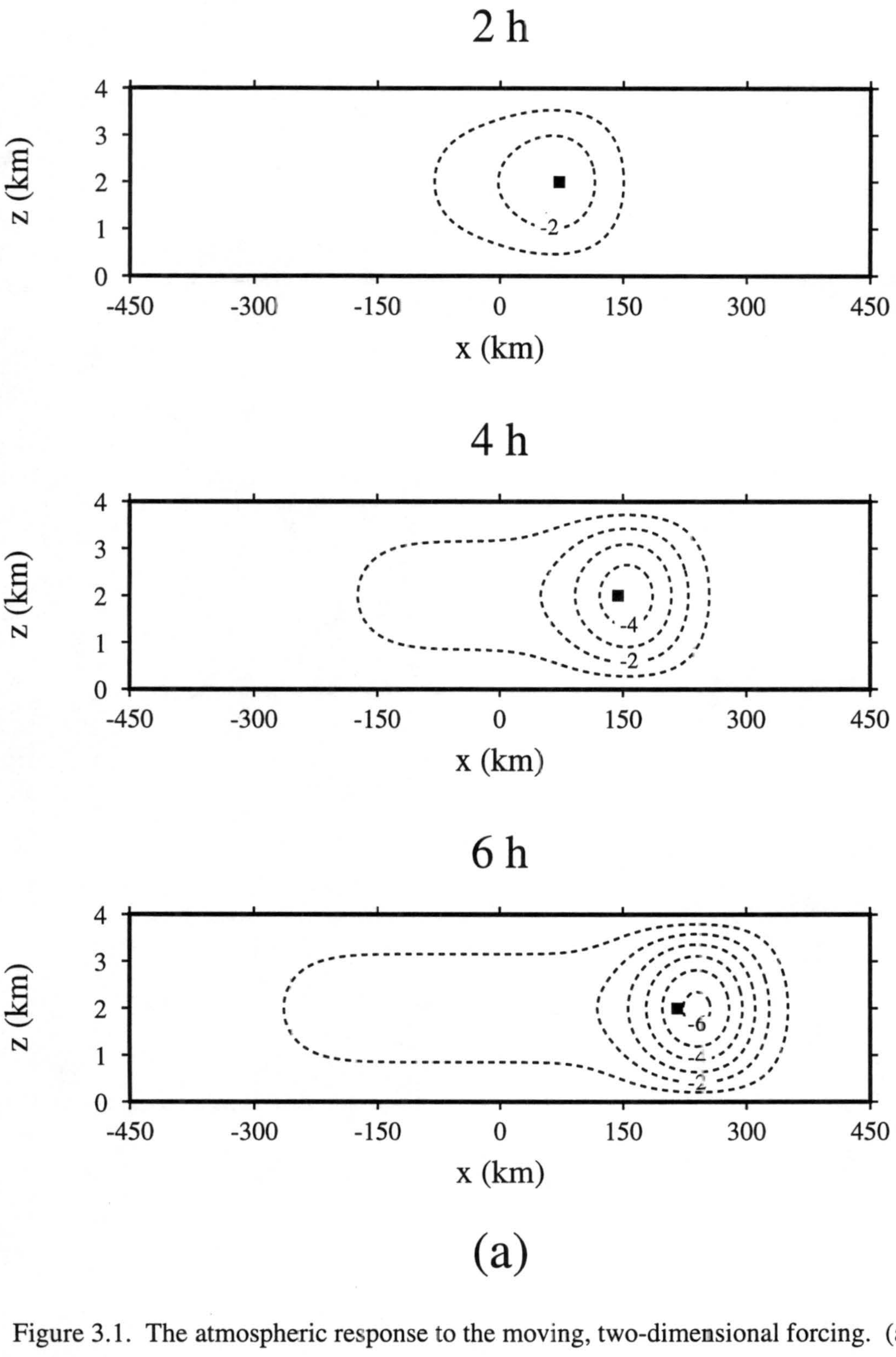

Figure 3.1. The atmospheric response to the moving, two-dimensional forcing. (a) perturbation temperature with a 1 K contour interval. The maximum in forcing is marked with a solid box.

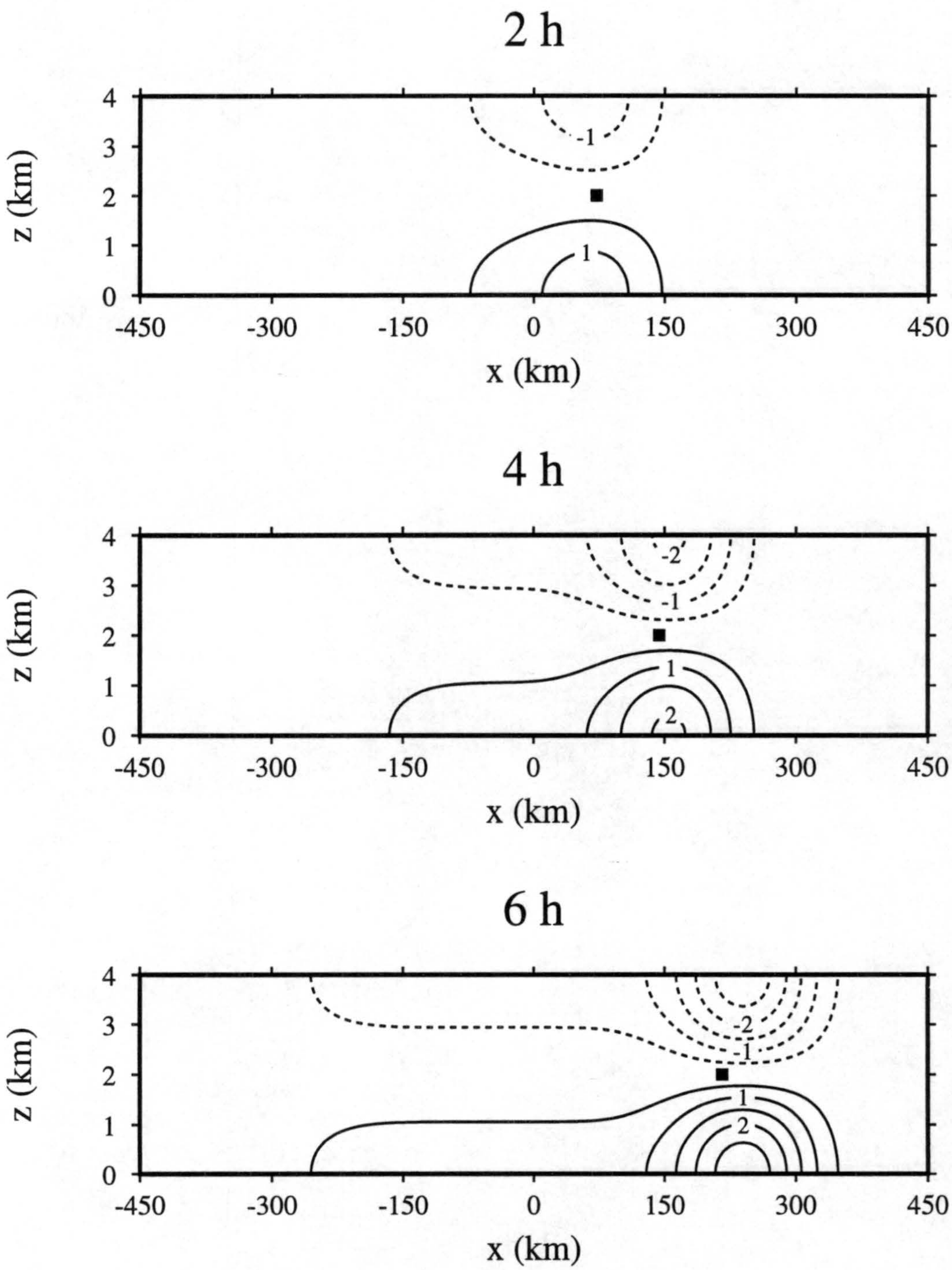

(b)

Figure 3.1 (continued). (b) perturbation pressure with a 0.5 hPa contour interval. The zero contours are omitted.

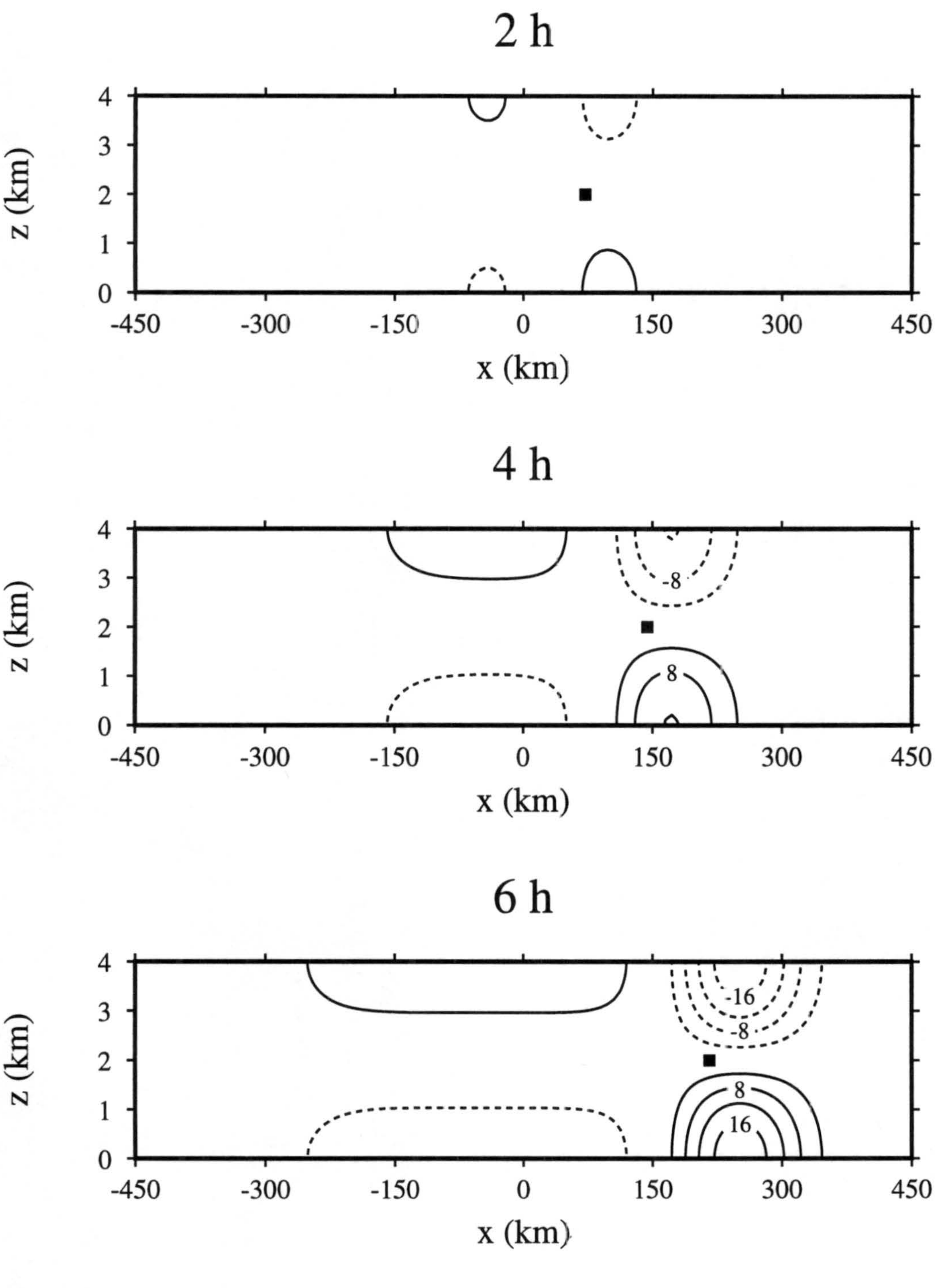

(c)

Figure 3.1 (continued). (c) perturbation wind with a 4 m s^{-1} contour interval. The zero contours are omitted.

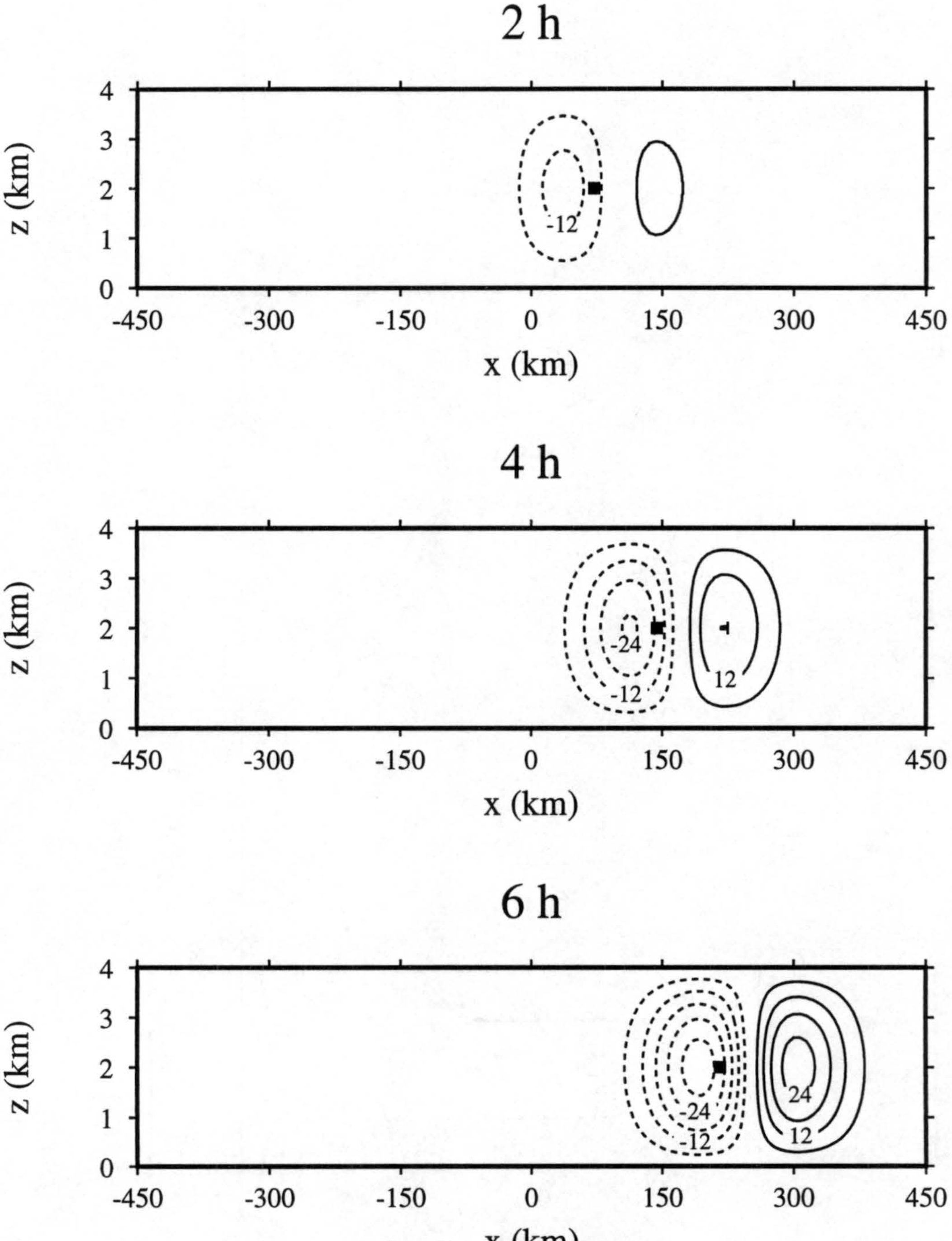

(d)

Figure 3.1 (continued). (d) vertical velocity with a 6 cm s^{-1} contour interval. The zero contours are omitted.

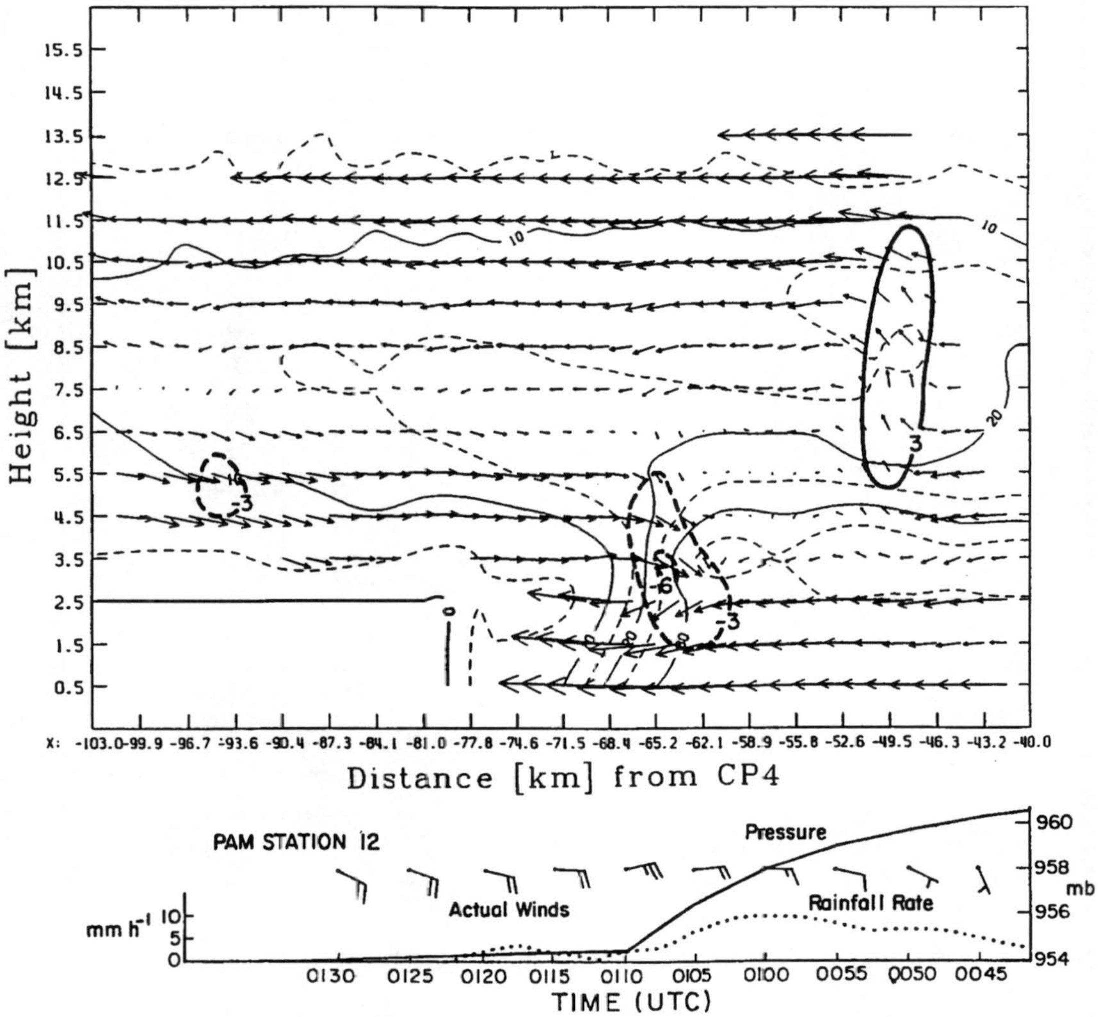

Figure 3.2. A vertical cross section of radar reflectivity (dBZ, narrow lines), dual-Doppler system-relative winds (vectors) and vertical motion (m s^{-1}, wide lines) through a squall system over Kansas at 0107 UTC 4 June 1985 (top); and time-to-space converted observations of pressure, wind, and rainfall rate from a surface station in the vicinity of the radar measurements (bottom) (from Stumpf et al. 1991).

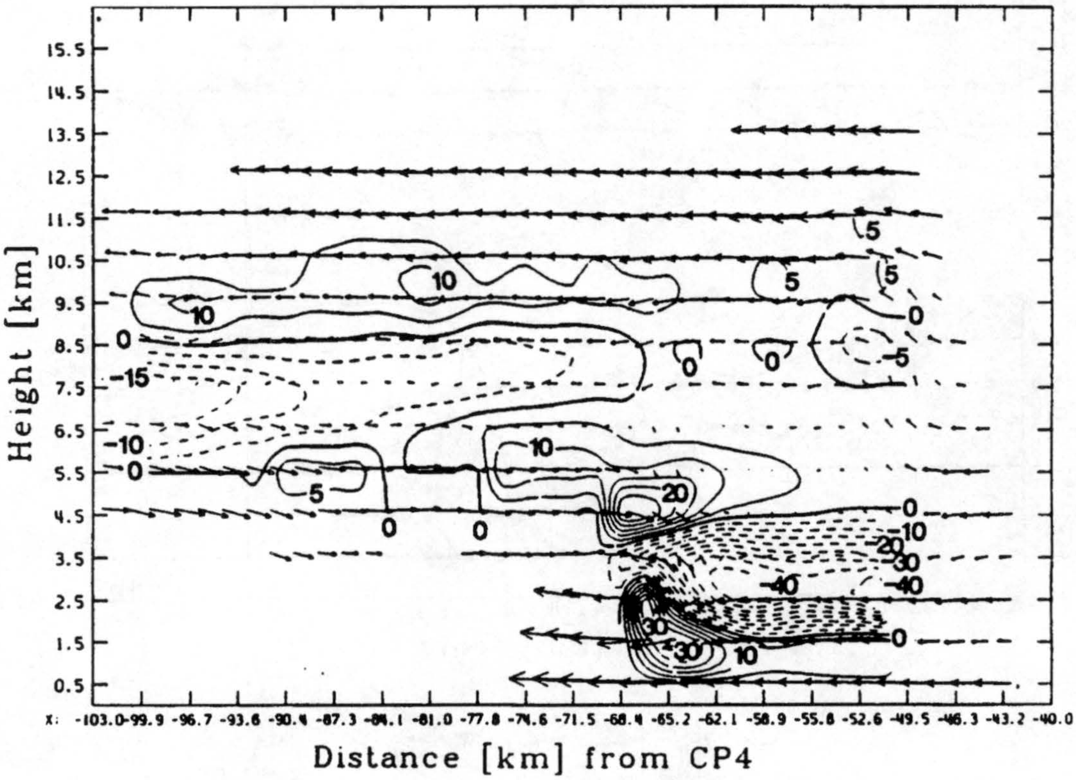

Figure 3.3. A vertical cross section of perturbation buoyancy (labeled in tenths of ^{o} K) which corresponds to Figure 3.2 (from Smull and Jorgensen 1990).

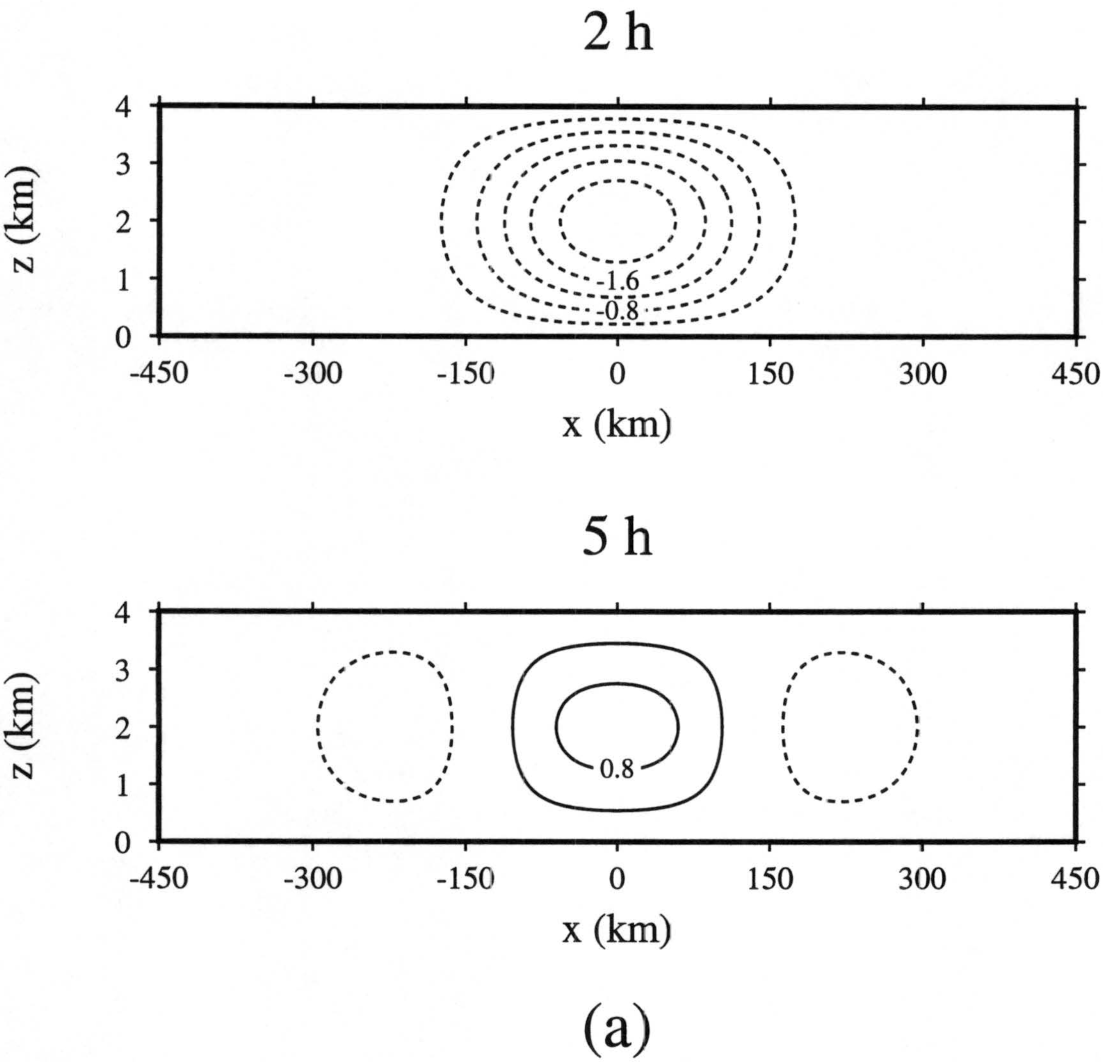

Figure 3.4. A vertical cross-section (along $y = 0$) of the atmospheric response to the stationary, three-dimensional forcing. (a) perturbation temperature with a 0.4 K contour interval. The zero contours are omitted.

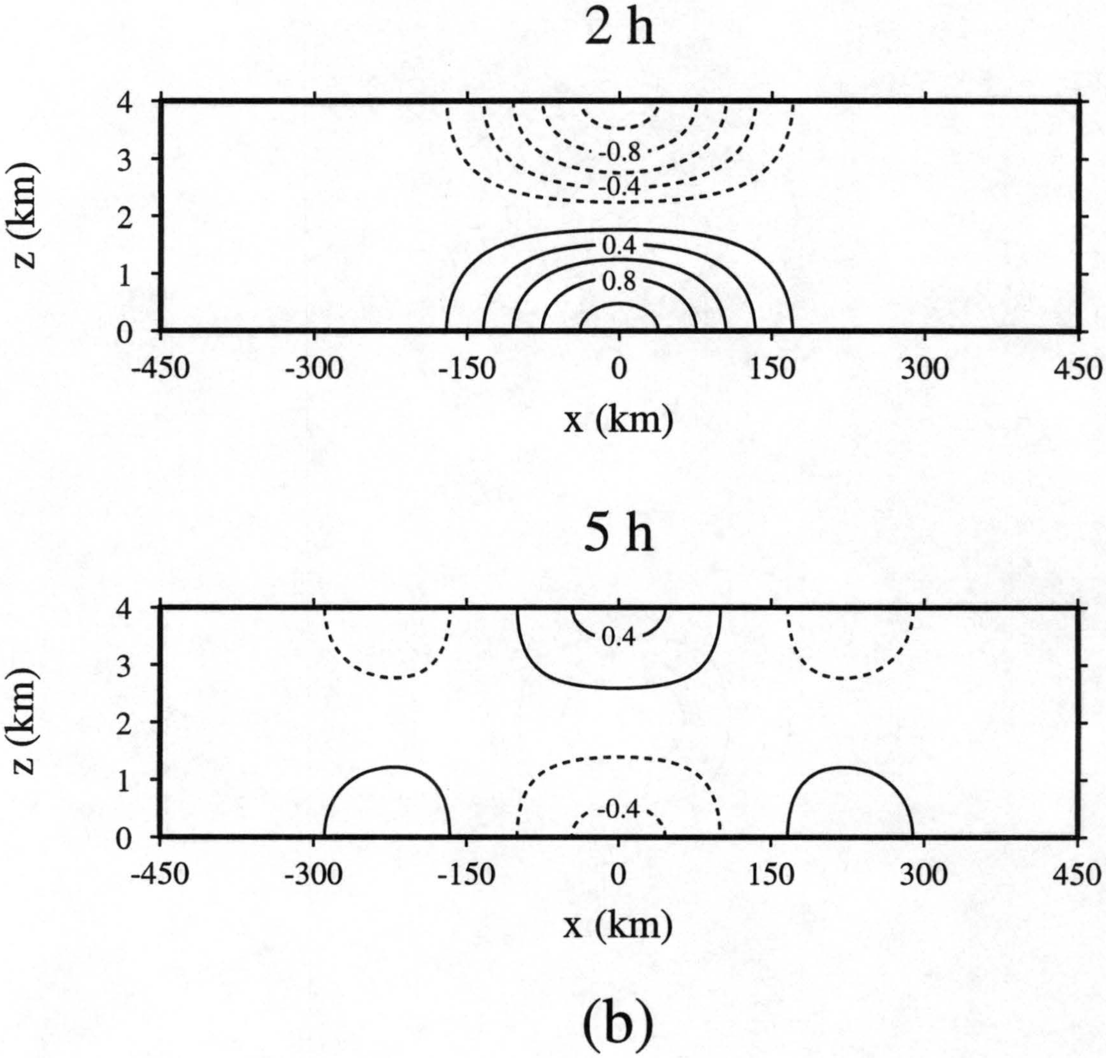

Figure 3.4 (continued). (b) perturbation pressure with a 0.2 hPa contour interval. The zero contours are omitted.

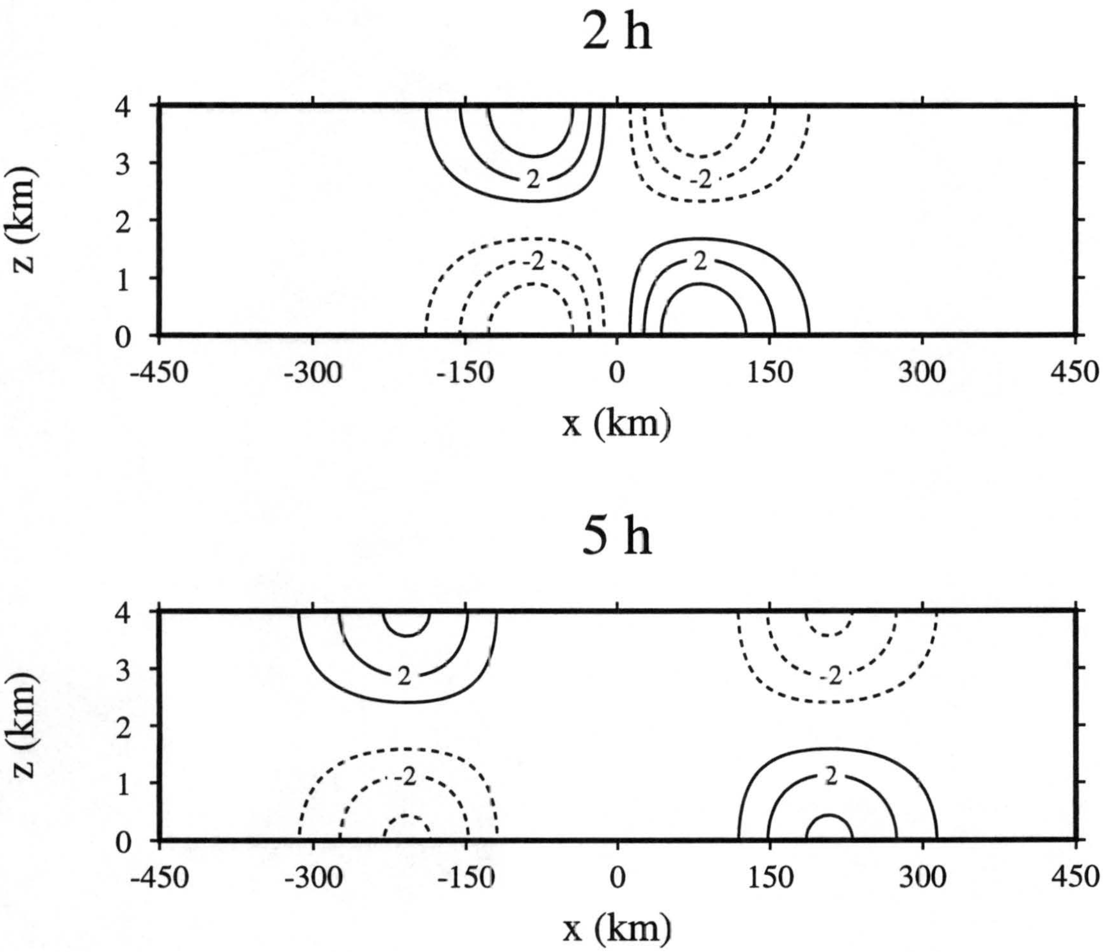

(c)

Figure 3.4 (continued). (c) perturbation zonal wind with a 1 m s^{-1} contour interval. The zero contours are omitted.

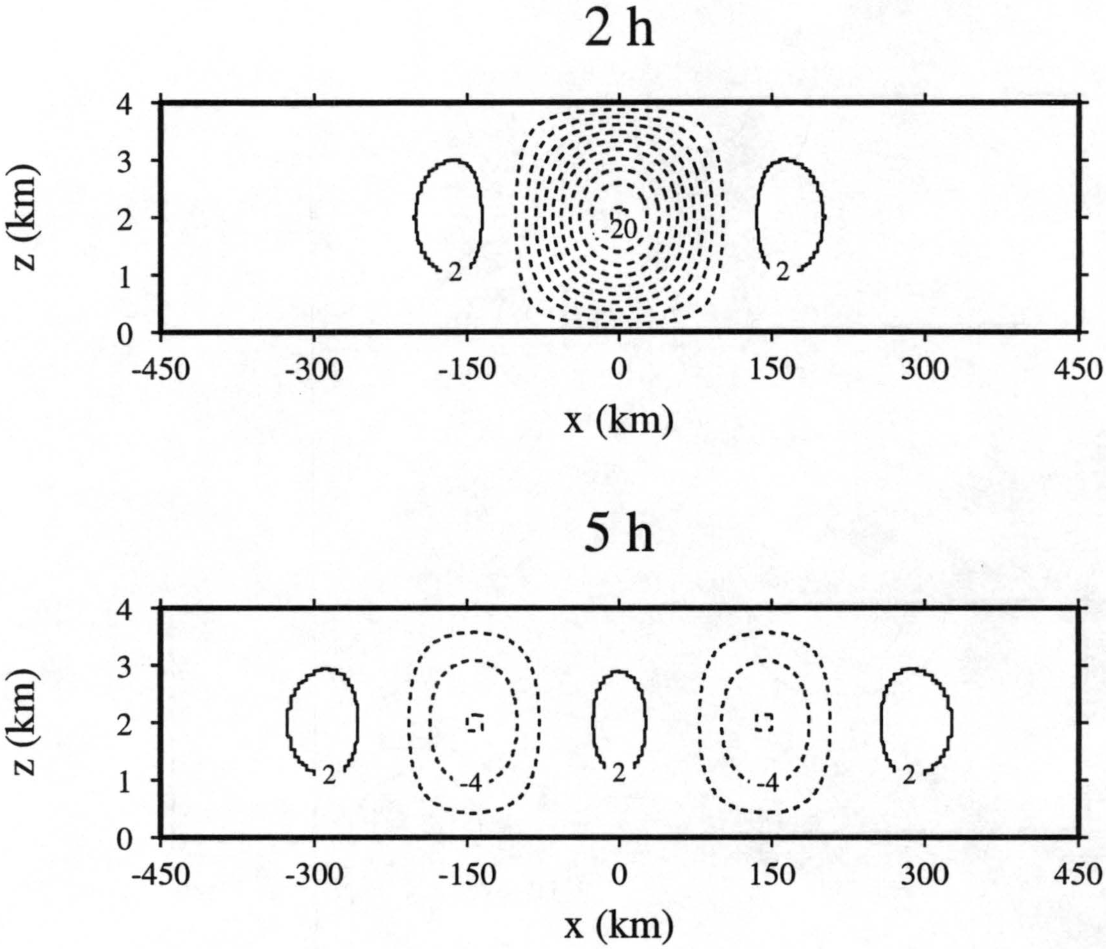

(d)

Figure 3.4 (continued). (d) vertical velocity with a 2 cm s^{-1} contour interval. The zero contours are omitted.

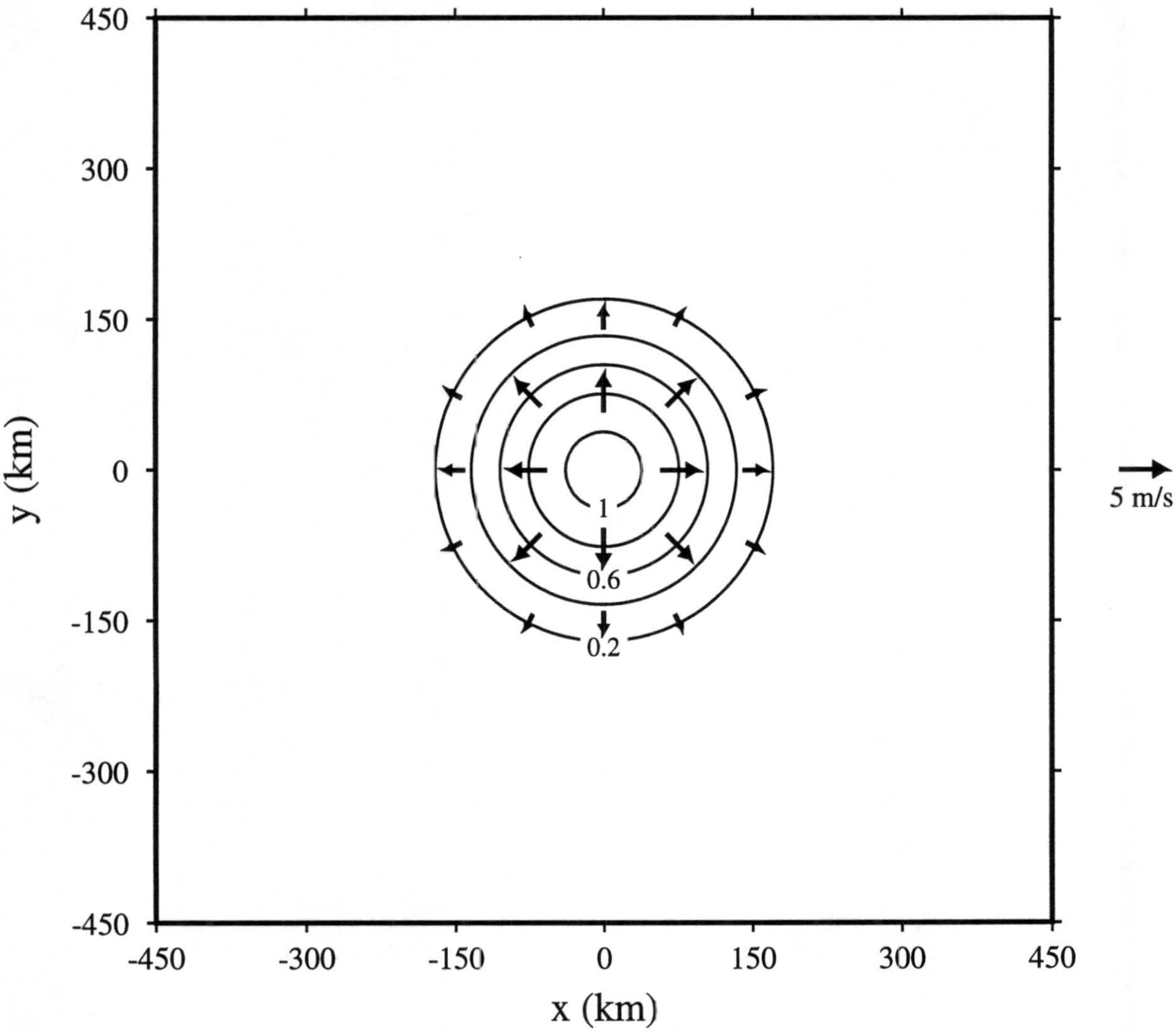

(a)

Figure 3.5. The atmospheric response at the surface to the stationary, three-dimensional forcing. (a) perturbation pressure and winds at 2 h. The countour interval is 0.2 hPa and the zero contours are omitted.

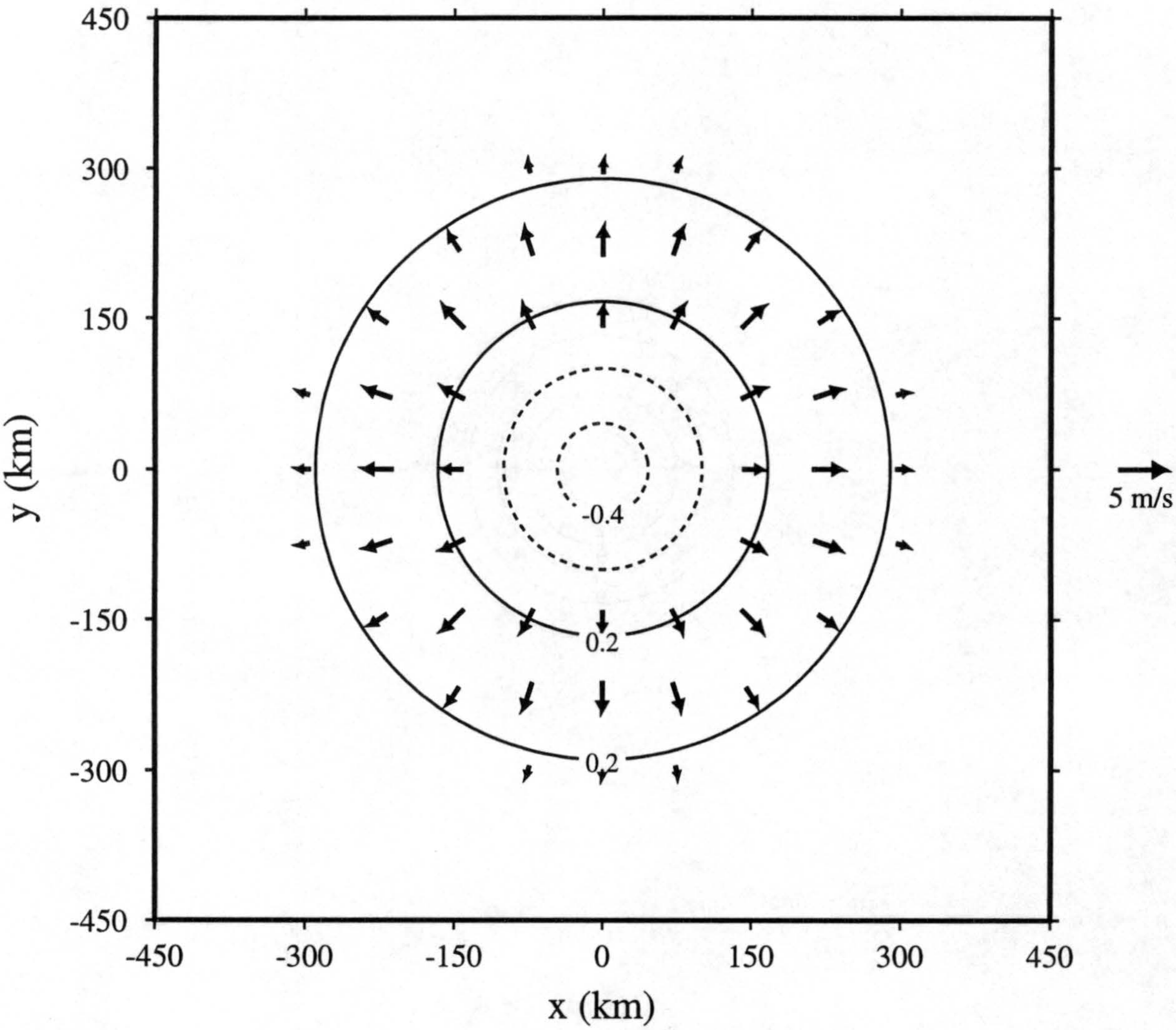

(b)

Figure 3.5 (continued). (b) perturbation pressure and winds at 5 h contoured as before.

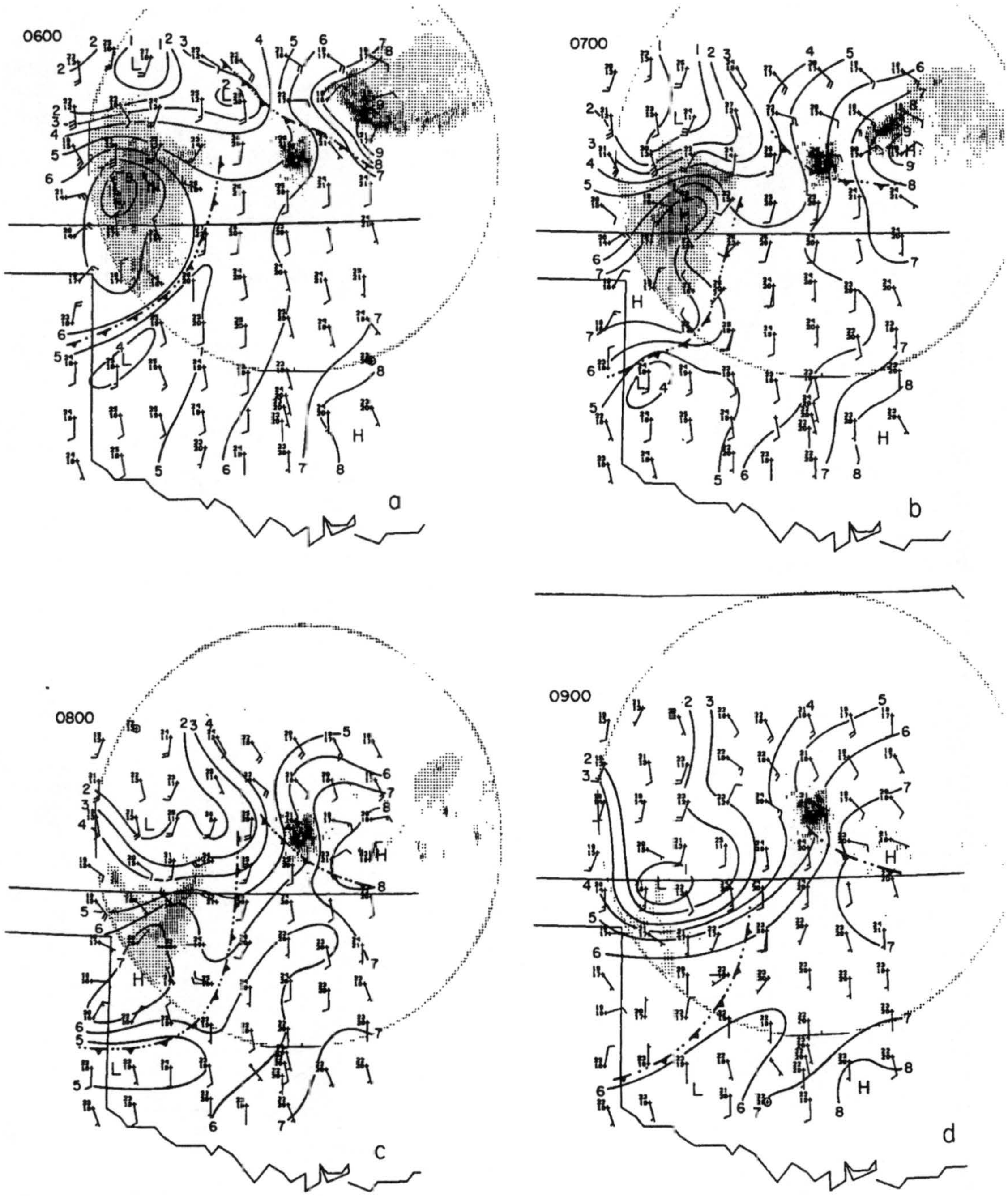

Figure 3.6. Surface analysis at 0600, 0700, 0800 and 0900 UTC on 24 June 1985 over portions of Kansas, Oklahoma, and the Texas Panhandle. Contours represent the departure of 518 m pressure from 950 mb. Temperatures and dew points are in degrees C. Radar reflectivity is shaded with thresholds of 18, 30, 40, 45, and 50 dBZ (from Johnson et al. 1989).

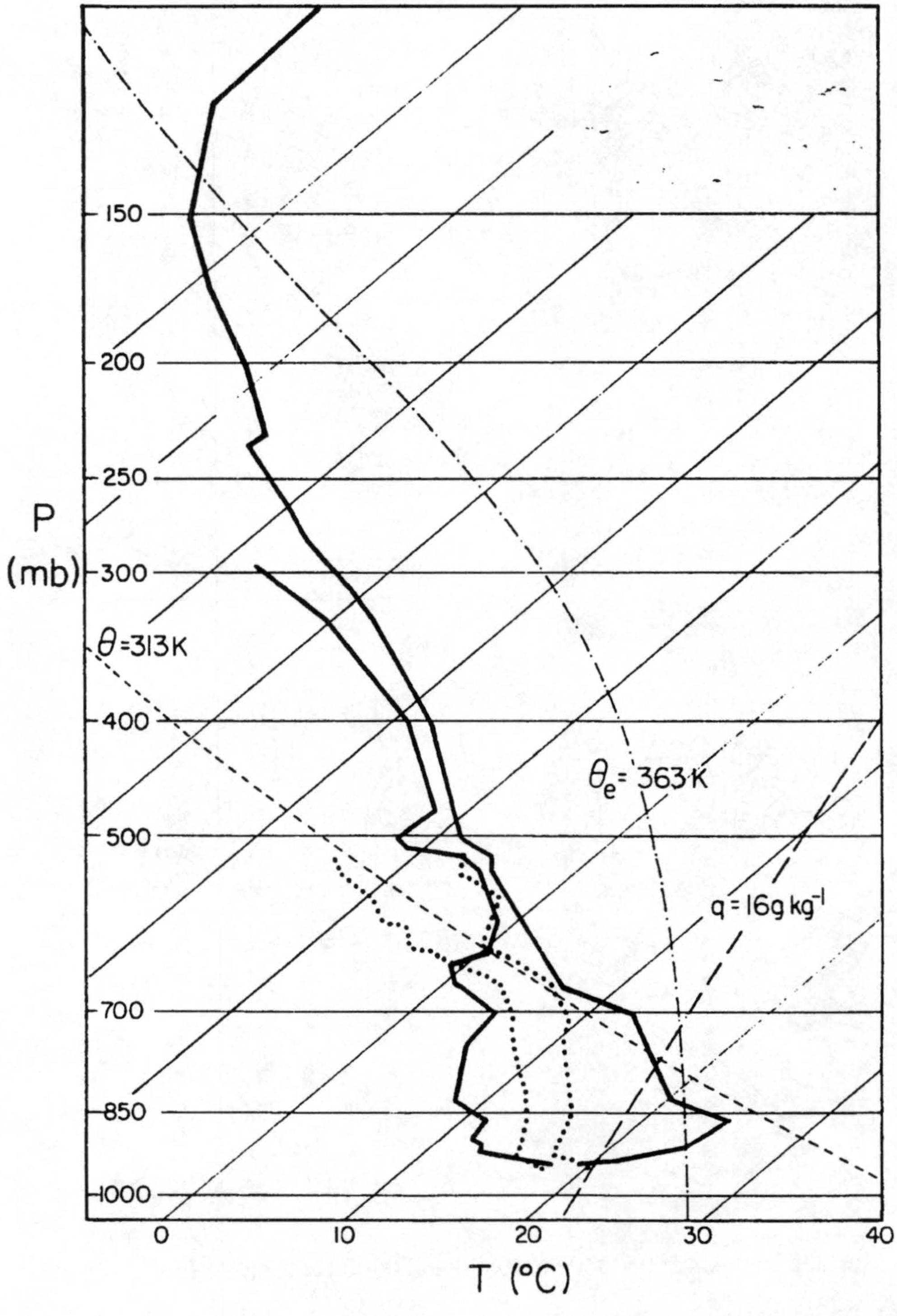

Figure 3.7. Temperature and dewpoint above Woodward, Oklahoma at 0600 (solid) and 0855 (dashed) UTC on 24 June 1985 (from Johnson et al. 1989).

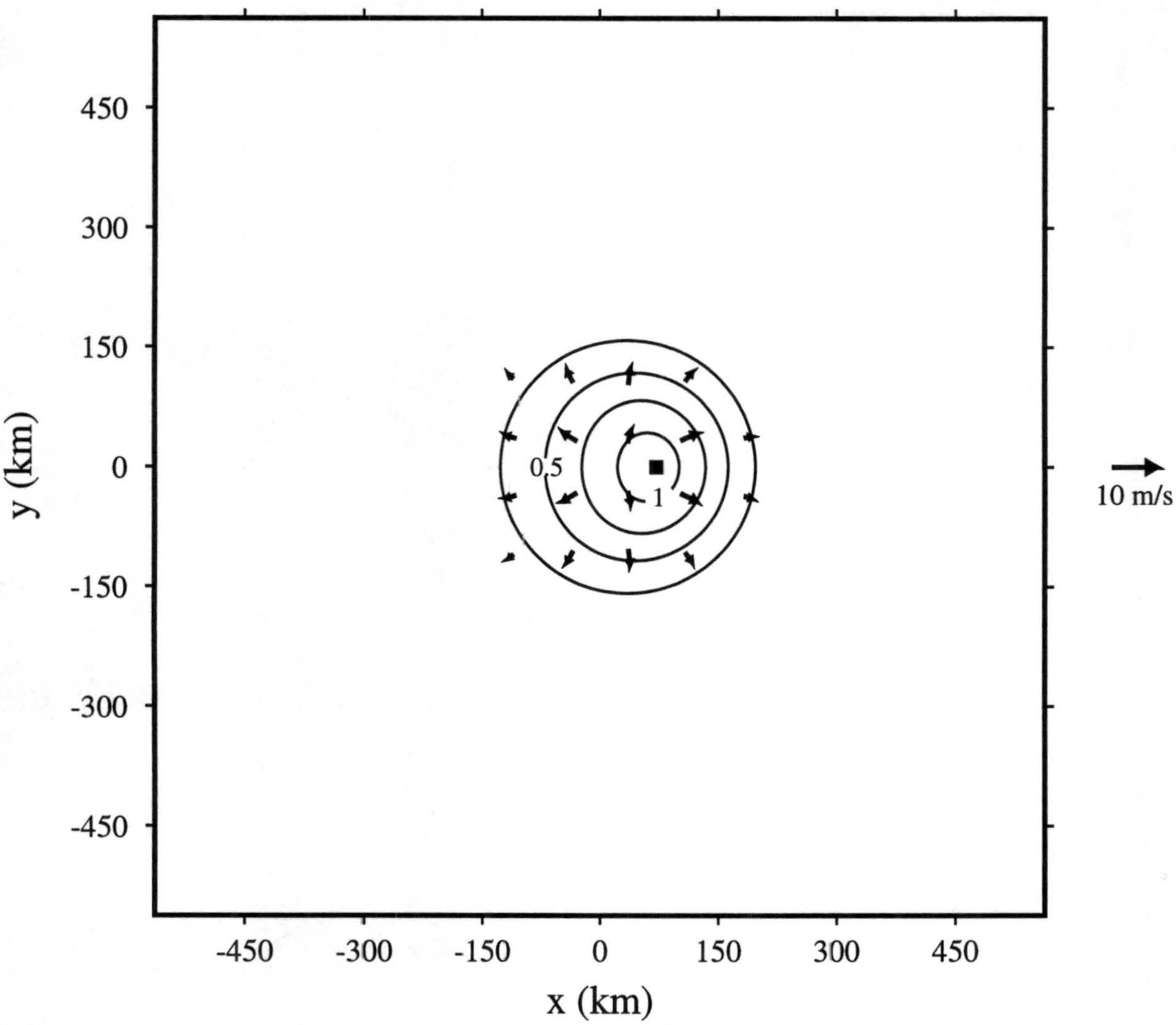

(a)

Figure 3.8. The atmospheric response at the surface to the moving, three-dimensional forcing. (a) perturbation pressure and winds at 2 h. The contour interval is 0.25 hPa. The maximum in forcing is marked with a solid box.

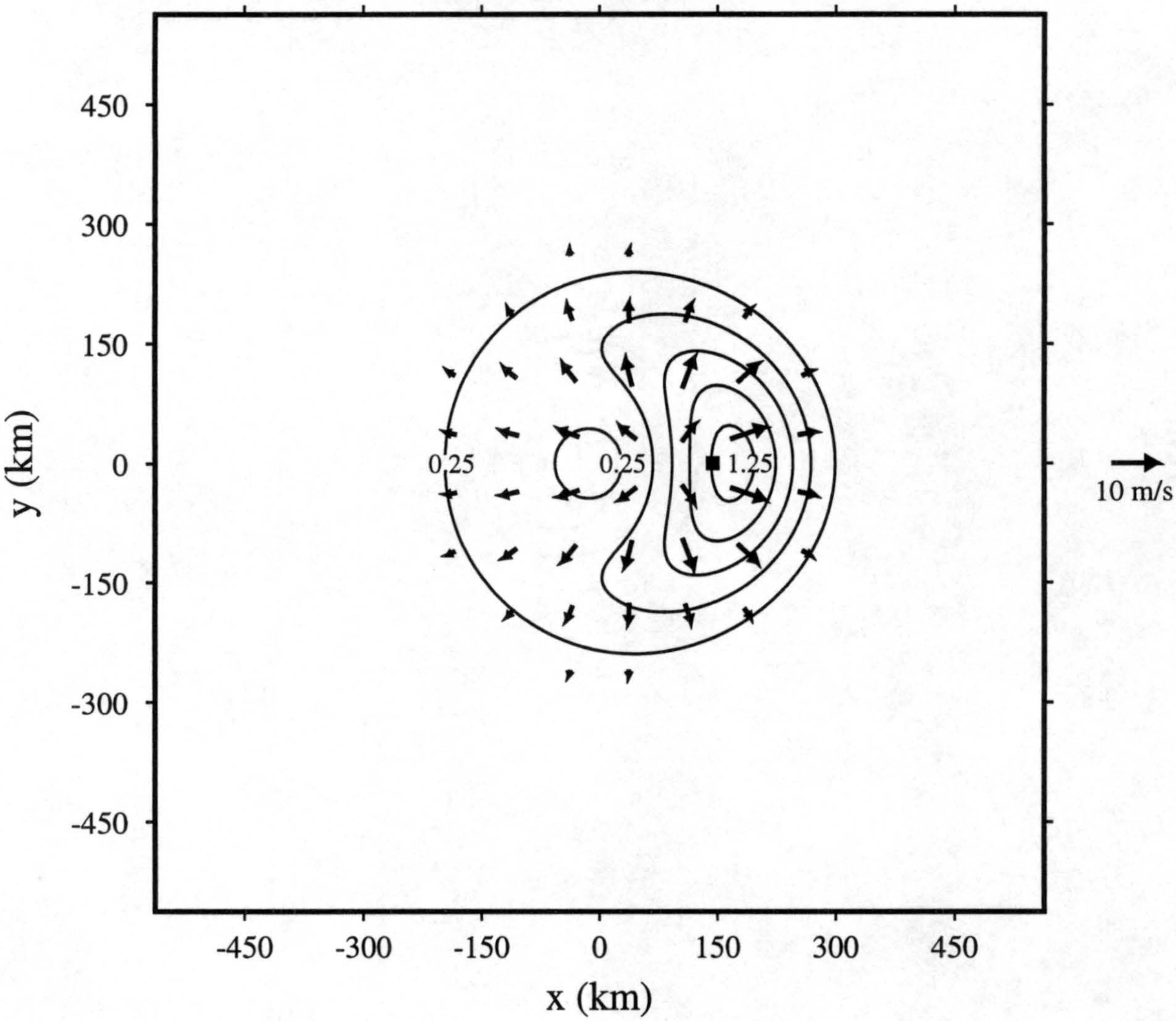

(b)

Figure 3.8 (continued). (b) perturbation pressure and winds at 4 h contoured as before.

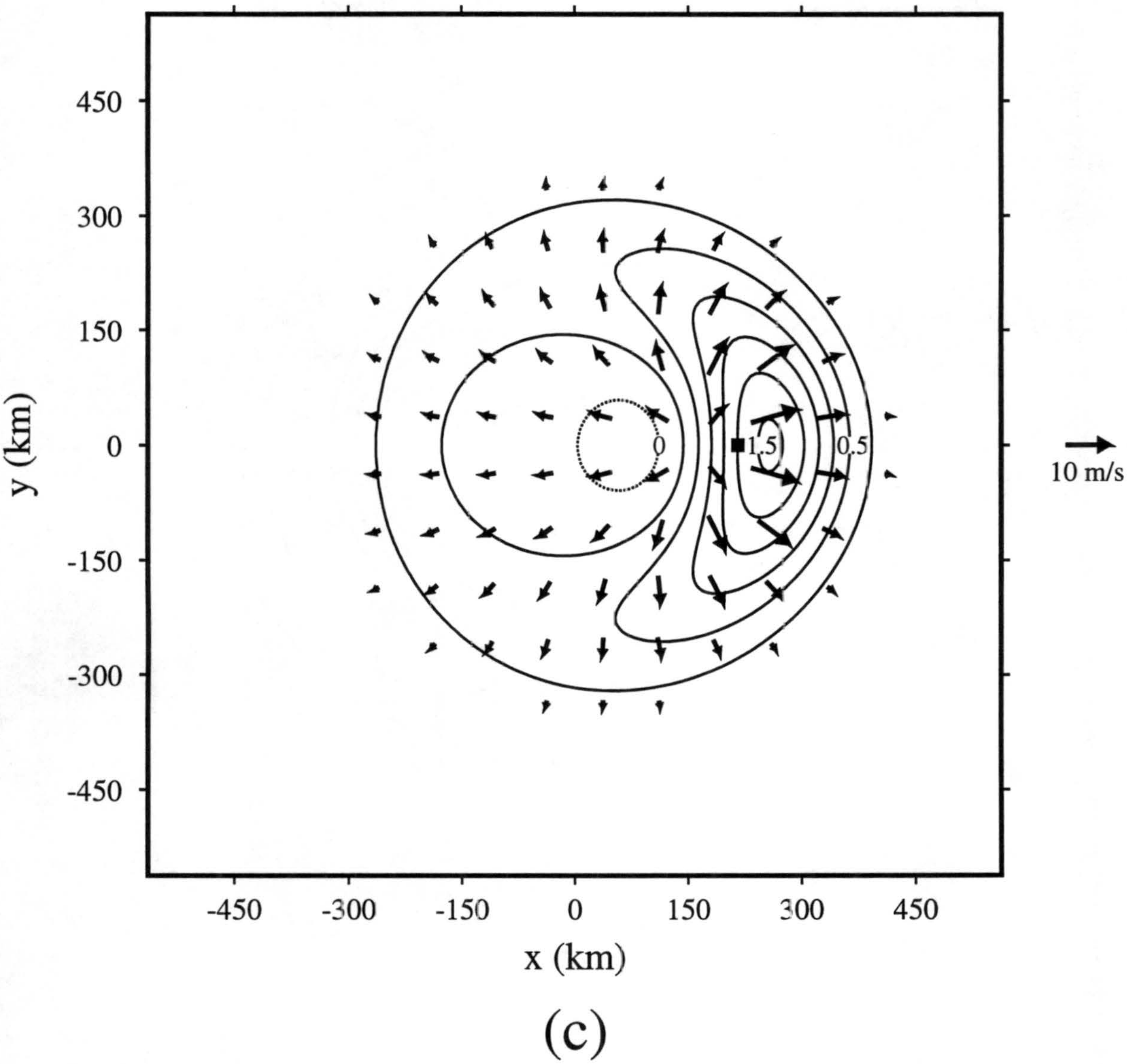

Figure 3.8 (continued). (c) perturbation pressure and winds at 6 h contoured as before.

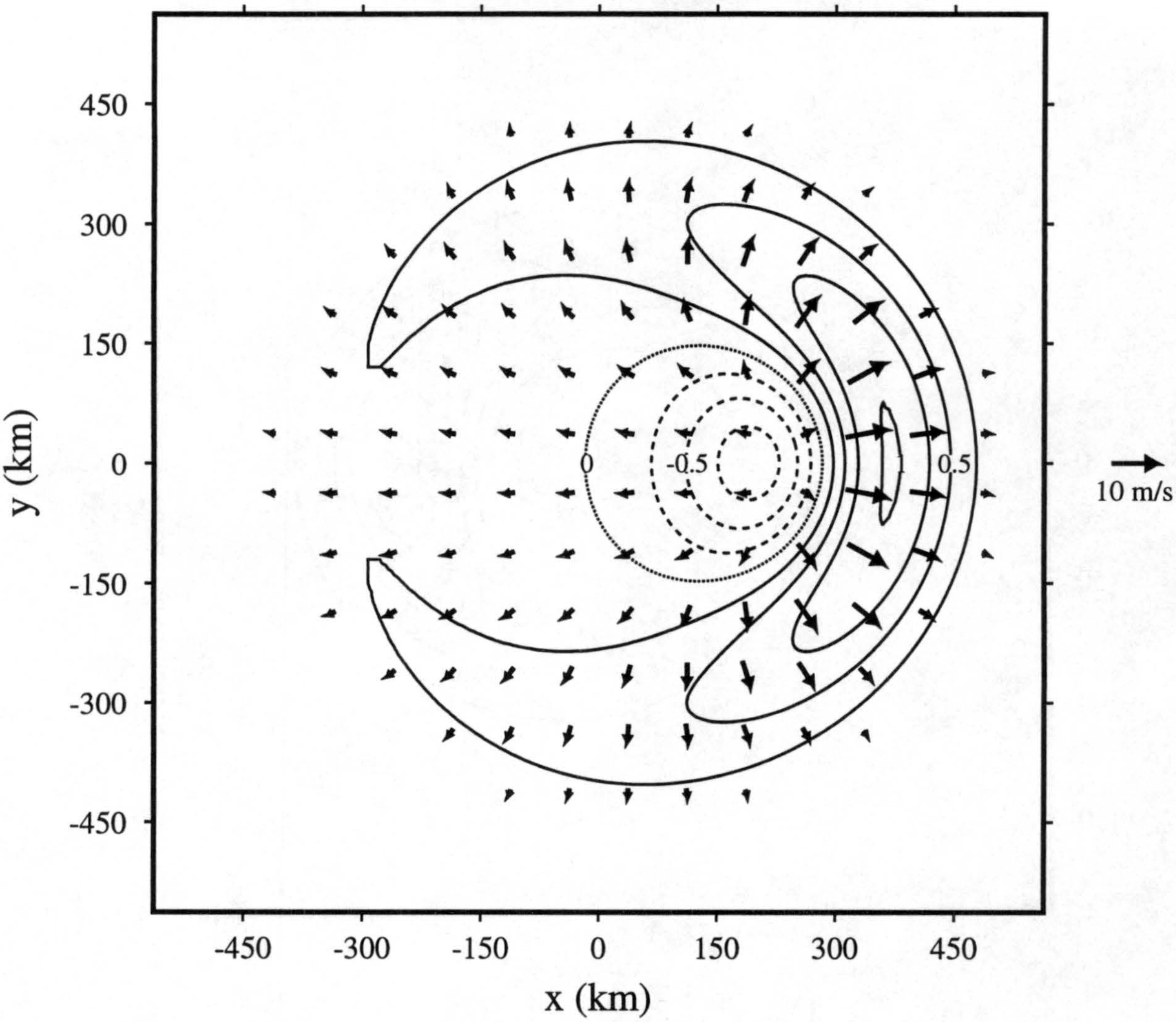

(d)

Figure 3.8 (continued). (d) perturbation pressure and winds at 8 h contoured as before.

Chapter 4

THE STEADY-STATE RESPONSE

In this chapter we use mathematics to analyze the buoyancy-wave response to the low-level cooling associated with stratiform precipitation. When the cooling moves at a constant speed, within its frame of reference the response approaches a steady state. We solve for the steady-state response to each of two moving forcings.

Suppose that the forcing is initially centered at the origin and that it moves at a speed c in the x-direction. Let $\tilde{x}$ represent the x-distance from a point to the center of the forcing so $\tilde{x} = x - ct$. If we choose a new coordinate system in which x is replaced by $\tilde{x}$ the system (3.3-3.7) becomes:

$$\frac{\partial u}{\partial t} + \bar{u}\frac{\partial u}{\partial \tilde{x}} + \frac{1}{\rho_0}\frac{\partial p}{\partial \tilde{x}} = 0 \tag{4.1}$$

$$\frac{\partial v}{\partial t} + \bar{u}\frac{\partial v}{\partial \tilde{x}} + \frac{1}{\rho_0}\frac{\partial p}{\partial y} = 0 \tag{4.2}$$

$$\frac{1}{\rho_0}\frac{\partial p}{\partial z} = b \tag{4.3}$$

$$\frac{\partial b}{\partial t} + \bar{u}\frac{\partial b}{\partial \tilde{x}} + wN^2 = Q \tag{4.4}$$

$$\frac{\partial u}{\partial \tilde{x}} + \frac{\partial v}{\partial y} + \frac{\partial w}{\partial z} = 0 \tag{4.5}$$

where $\bar{u} = -c$ and the other variables are as before. Following the procedure discussed in Chapter 2 we reduce the system to non-dimensional shallow water equations:

$$\frac{\partial \hat{u}'}{\partial t'} + \bar{u}' \frac{\partial \hat{u}'}{\partial \tilde{x}'} + \frac{\partial \hat{p}'}{\partial \tilde{x}'} = 0 \tag{4.6}$$

$$\frac{\partial \hat{v}'}{\partial t'} + \bar{u}' \frac{\partial \hat{v}'}{\partial \tilde{x}'} + \frac{\partial \hat{p}'}{\partial y'} = 0 \tag{4.7}$$

$$\frac{\partial \hat{p}'}{\partial t'} + \bar{u}' \frac{\partial \hat{p}'}{\partial \tilde{x}'} + \frac{\partial \hat{u}'}{\partial \tilde{x}'} + \frac{\partial \hat{v}'}{\partial y'} = \hat{Q}' \tag{4.8}$$

where $\bar{u}'$, y', $\hat{v}$ and $\hat{v}'$ are defined by the following equations:

$$\bar{u}' = \frac{m_0}{N} \bar{u} \tag{4.9}$$

$$y' = \frac{1}{[x]} y \tag{4.10}$$

$$v(\tilde{x}, y, z, t) = -\hat{v}(\tilde{x}, y, t) \cos(m_0 z) \tag{4.11}$$

$$\hat{v}' = \frac{m_0}{N} \hat{v} \tag{4.12}$$

and the other variables are defined by (2.7-2.8) and (2.11-2.15) (modified slightly for the moving coordinate and to include the additional dimension).

In order to find the steady-state solution to (4.6-4.8) we set the time derivatives to zero and use (4.6) and (4.7) to eliminate $\hat{u}'$ and $\hat{v}'$ from (4.8) yielding the following equation:

$$\frac{\partial^2 \hat{p}'}{\partial \tilde{x}'^2} + \beta \frac{\partial^2 \hat{p}'}{\partial y'^2} = \alpha \frac{\partial \hat{Q}'}{\partial \tilde{x}'} \tag{4.13}$$

where $\alpha = \dfrac{-\bar{u}'}{1-\bar{u}'^2}$ and $\beta = \dfrac{1}{1-\bar{u}'^2}$ (here we have assumed $\bar{u}' \neq 1$). For a given forcing (4.13) does not uniquely determine $\hat{p}'$; adding a constant to a solution yields another solution. If we assume that the forcing vanishes at infinite distance we expect the solution to also vanish at infinite distance, and this boundary condition uniquely determines $\hat{p}'$. Making use of this boundary condition we also solve for $\hat{u}'$ and $\hat{v}'$ in terms of $\hat{p}'$ using (4.6) and (4.7):

$$\hat{u}' = -\frac{1}{\bar{u}'}\,\hat{p}' \tag{4.14}$$

$$\hat{v}' = -\frac{1}{\bar{u}'}\int_{-\infty}^{\tilde{x}'} \frac{\partial \hat{p}'}{\partial y'}\,d\eta \tag{4.15}$$

where η is a dummy variable used to represent integration over $\tilde{x}'$.

We now solve (4.13-4.15) for a moving, three-dimensional stratiform cooling:

$$Q(\tilde{x}, y, z, t) = Q_0\; Q_{xy}(\tilde{x}, y)\,\sin(m_0 z) \tag{4.16}$$

where Q_0, Q_{xy}, m_0 and c are as in Section 3.3. This forcing differs from the one defined by (3.9) in that it never shuts off. We evaluate the right-hand side of (4.13) analytically and approximate the terms on the left-hand side using finite differences where $\hat{p}'$ is defined on a grid spaced so that $\Delta y = \Delta\tilde{x}\sqrt{\beta}$. The resulting difference equation is as follows:

$$\hat{p}'_{i-1,j} + \hat{p}'_{i+1,j} + \hat{p}'_{i,j-1} + \hat{p}'_{i,j+1} - 4\hat{p}'_{i,j} = (\Delta\tilde{x})^2\,\alpha\,\frac{\partial \hat{Q}'}{\partial \tilde{x}'} \tag{4.17}$$

where i and j are indices in the $\tilde{x}$- and y-directions respectively. We solve (4.17) using Gauss-Seidel relaxation with $\Delta\tilde{x} = 0.1$. We then use (4.14) and (4.15) to solve for $\hat{u}'$ and $\hat{v}'$ in terms of $\hat{p}'$. We approximate the integral in (4.15) using a Riemann sum.

The steady-state response includes a mesohigh ahead of the forcing and a wake low trailing the forcing (Figure 4.1). Westerlies accompany the mesohigh and easterlies accompany the mesolow. Both the easterlies and the westerlies diverge in the y-direction. There is a remarkable resemblence between this response and the schemata constructed by Johnson and Hamilton (1988) and Loehrer and Johnson (1995) (Figures 1.1 and 1.3). The mesohigh and wake low within the steady-state response are each less intense than their counterparts in the schemata, but most of the difference in intensity is attributable to the y-scale of the forcing and our conservative choice of Q_0. When the y-scale of the forcing is doubled and Q_0 is set to -2.99×10^{-5} m s^{-3} (3 K h^{-1}), the steady-state response includes a mesohigh and a wake low which each have an intensity of greater than 2 hPa (not shown).

The solution shown in Figure 4.1 represents the atmospheric response to the forcing at infinite time. So how quickly does the transient solution approach this steady-state solution? To answer this question we take another look at the numerical simulation presented in Section 3.3. After four hours the transient solution includes a dipole response in surface pressure (Figure 3.8(b)). After six hours there is a strong resemblence between the transient and the steady-state solutions, and the difference in pressure between the center of the mesohigh and the center of the wake low is approximately what it is in the steady-state solution (Figures 3.8(c) and 4.1). However, the mean perturbation pressure in the vicinity of the forcing is primarily positive in the transient solution, whereas it is zero in the steady-state solution. When the forcing is allowed to continue after six hours the mean pressure in its vicinity gradually decreases with time (not shown). We conclude that in a matter of hours the transient solution may be first be interpreted as a quasi-steady-state response.

We have solved equation (4.13) for a particular thermal forcing. This equation may also be used to qualitatively describe the surface-pressure response to a general thermal forcing. For a typical forcing (with $\bar{u}' < 1$) the constant β is on the order of 1, so the terms on the left-hand side are like a Laplacian of $\hat{p}'$, and their sum is roughly proportional to the negative of $\hat{p}'$. By equations (2.8) and (2.14), $\hat{p}'$ is proportional to the negative of surface-pressure, so the sum of the terms on the left-hand side of (4.13) is roughly proportional to the surface pressure. It follows that (4.13) predicts a surface-pressure response which is roughly proportional to the gradient in the forcing in the direction of its movement. This conclusion applies to the response shown in Figure 4.1. On the western (eastern) edge of the forcing there is a negative (positive) gradient in the forcing in the x-direction and low (high) pressure.

The intensity of the surface-pressure response predicted by (4.13) is proportional to α, which is a function of the non-dimensional wind $\bar{u}'$. The magnitude of $\bar{u}'$ is simply the ratio of the speed of the forcing to the buoyancy-wave speed. When the speed of the forcing is small compared to the buoyancy-wave speed ($\bar{u}' \ll 1$) α is small (Figure 4.2), and the steady-state response is weak. As the speed of the forcing approaches the buoyancy-wave speed ($\bar{u}' \rightarrow 1$) α becomes infinite. When ($\bar{u}' > 1$) equation (4.13) becomes hyperbolic rather than elliptic and the steady-state solution has a different character. The hyberbolic version of (4.13) may be useful for interpreting the fine structure of temperature profiles above wake lows (i.e. the warm anomalies shown in Figure 3.3) contributed by high wave-number vertical modes, but we leave that question for later studies. The solution of a hyperbolic equation similar to (4.13) is discussed by Geisler (1970). For the response shown in Figure 4.1, $\bar{u}' = 0.785$ and $\alpha = 2.04$.

The discussion in the previous paragraph explains why the low-level cooling associated with stratiform precipition usually has a bigger impact on surface pressure than the deep heating associated with convection. If a convective heating has a depth of 10 km the buoyancy-wave speed for the response to that heating is 31 m s^{-1} (assuming that we leave N unchanged). If such a forcing moves at 10 m s^{-1} then $\bar{u}' = 0.314$ and $\alpha = 0.28 \ll 2.04$. The steady-state response to a convective forcing with the same speed, horizontal scale and magnitude as the stratiform forcing is shown in Figure 4.3. It includes a weak low ahead of the forcing and a weak high trailing the forcing. The intensity of the surface-pressure response is about one-fifth that of the response to the stratiform forcing. By comparing Figure 4.3 with Figure 4.1 one may also assess the impact of the parameter β, which equals 1.1 for the convective case and 2.6 for the stratiform case. For the convective case the pressure features have a smaller y-scale than those in the stratiform case. Apparently, increasing the value of β serves to smooth the steady-state response in the y-direction. While the buoyancy-wave response to convective forcing probably contributes little to mesohighs and wake lows, it may explain the weak pre-squall low observed in many squall systems (e.g. Figure 1.1).

Within this chapter we have seen that the buoyancy-wave response to stratiform cooling that so closely resembles observations of mesohighs and wake lows may be interpreted as a quasi-steady-state response. The intensity of this response is quite sensitive to the speed of the forcing relative to the buoyancy-wave speed. It appears that stratiform cooling has a bigger impact on surface pressure than convective forcing because the buoyancy-wave speed of the response to the stratiform forcing is closer to the speed at which MCS's typically move.

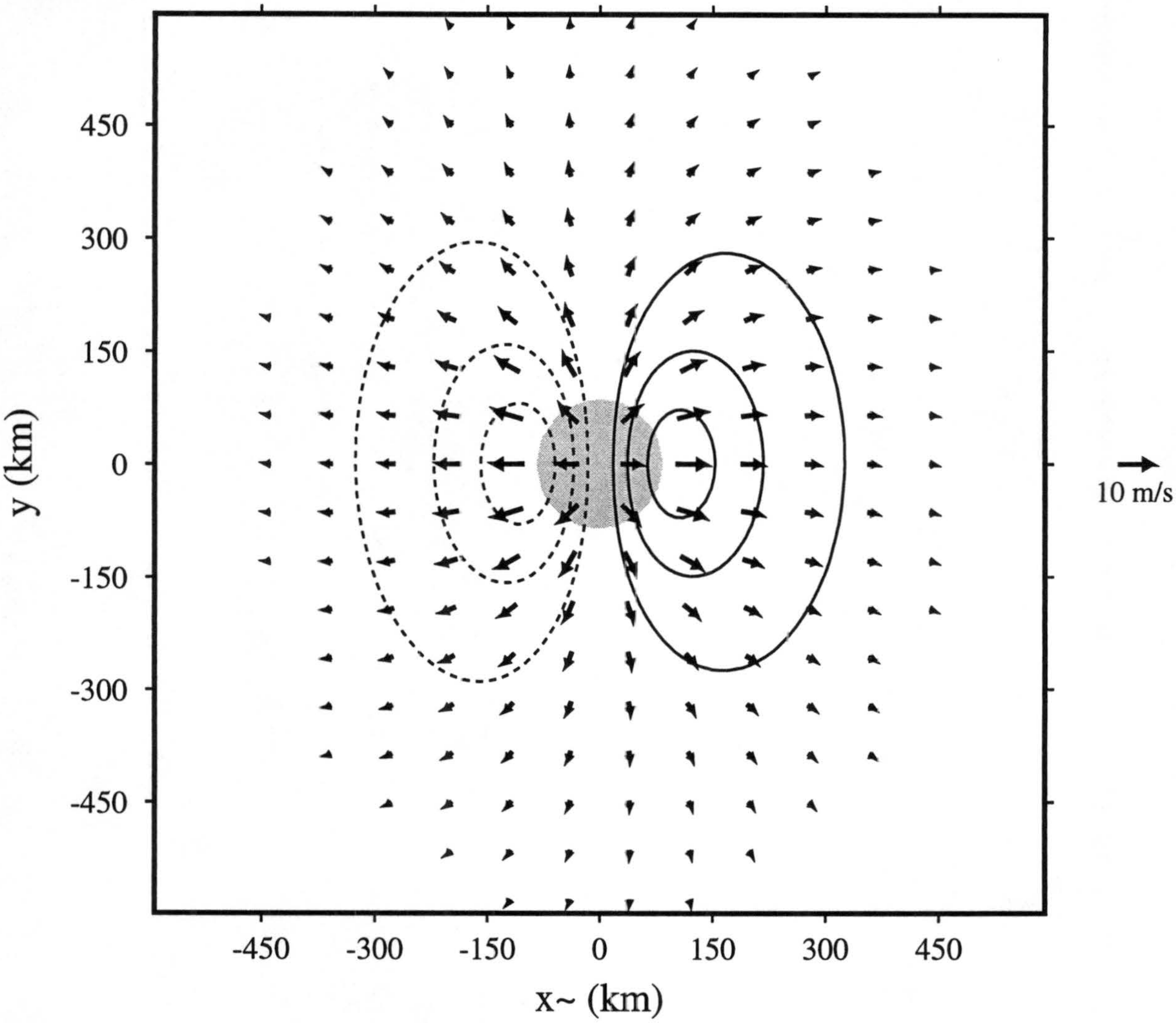

Figure 4.1. The steady-state response to the moving, three-dimensional stratiform forcing. Surface pressure is contoured with a 0.25 hPa contour interval and vectors represent surface winds. Positive contours are solid, negative contours are dashed, and the zero contour is omitted. The maximum cooling exceeds 1 K h^{-1} within the shaded region.

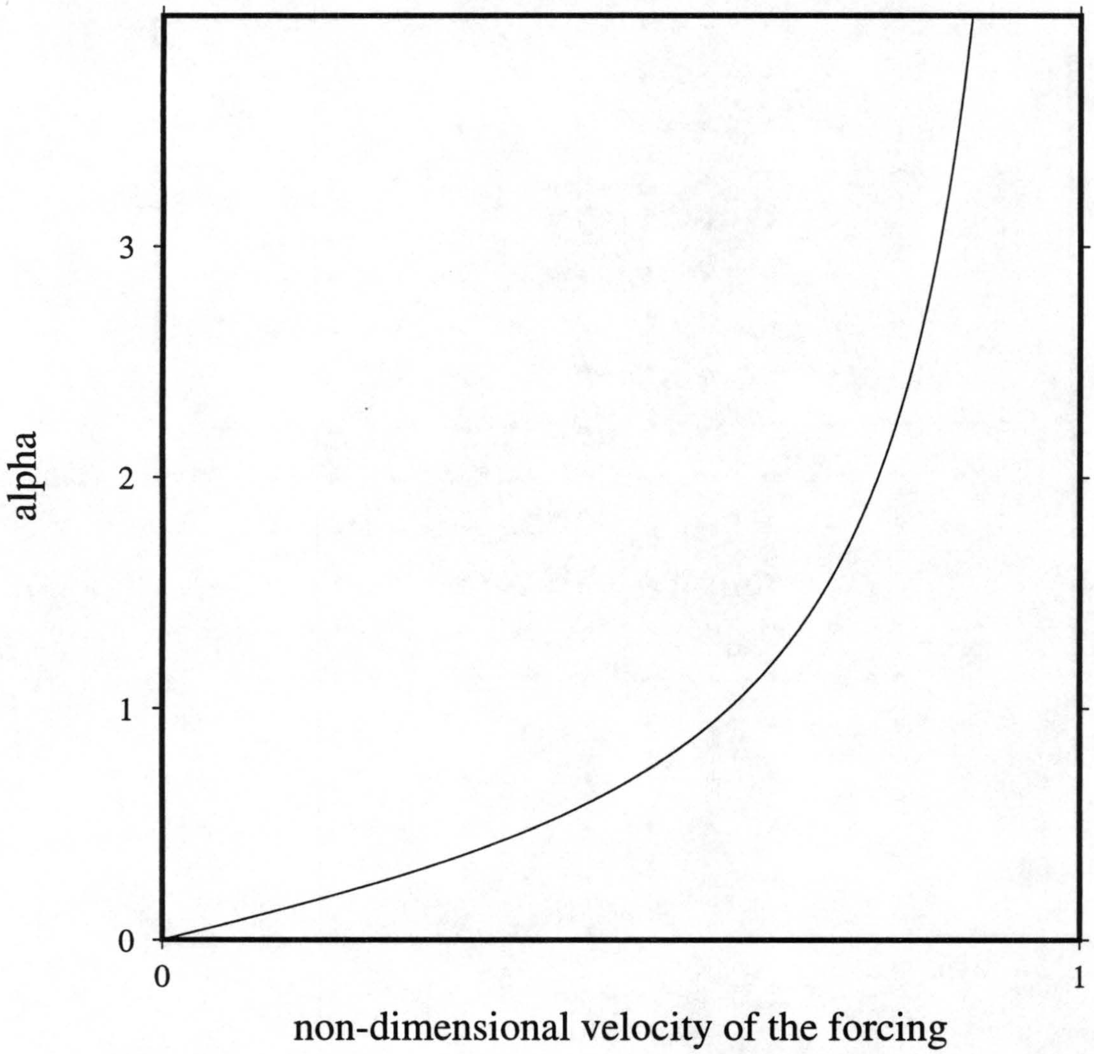

Figure 4.2. The proportionality constant α for the steady-state response to a moving thermal forcing.

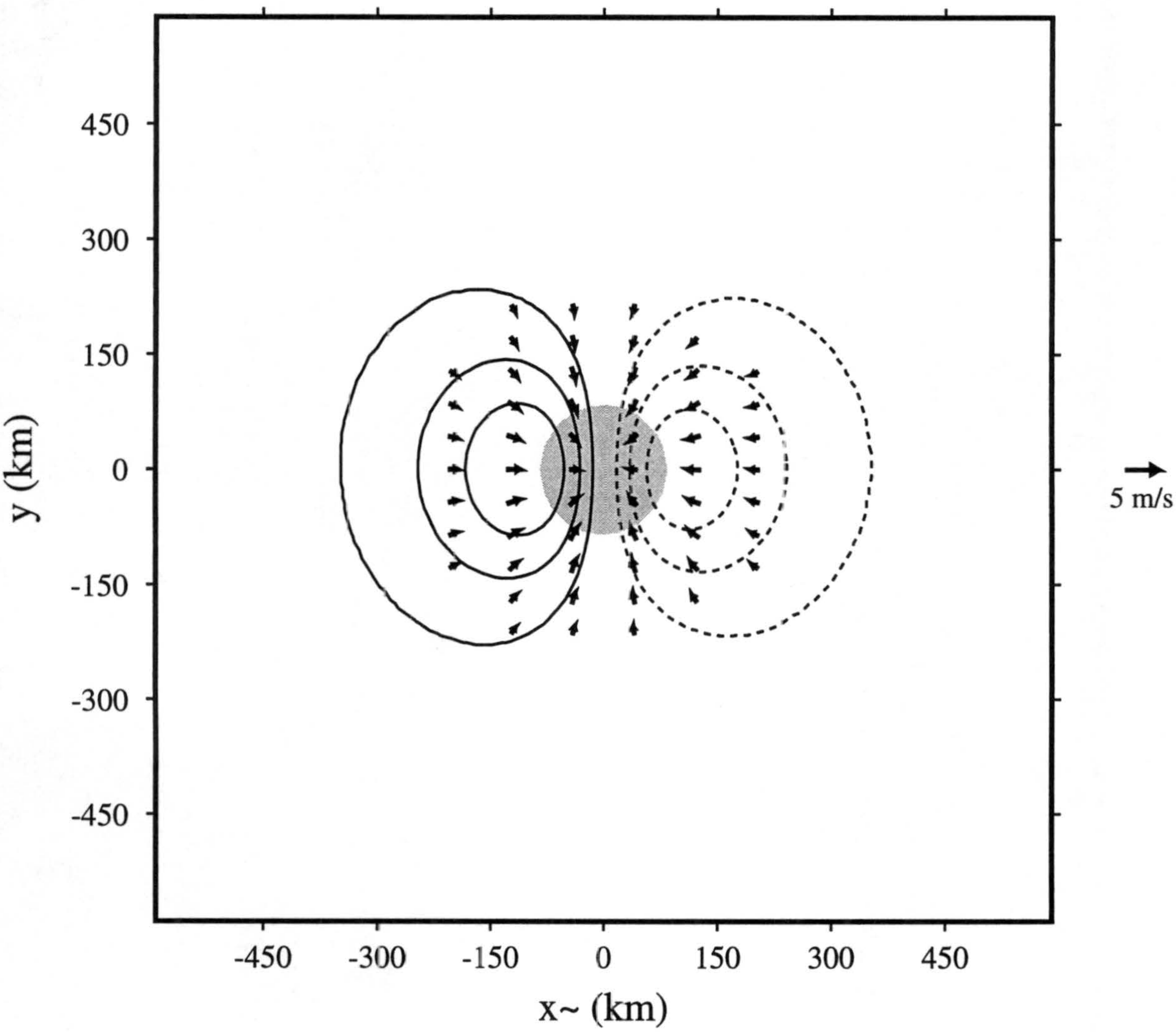

Figure 4.3. The steady-state response to the convective forcing. Surface pressure is contoured with a 0.05 hPa contour interval and vectors represent surface winds. Positive contours are solid, negative contours are dashed, and the zero contour is omitted. The maximum heating exceeds 1 K h^{-1} within the shaded region.

Chapter 5

SUMMARY AND DISCUSSION

Within this paper we have explored the idea that MCS mesohighs and wake lows are a buoyancy-wave response to the low-level cooling associated with stratiform precipitation. We used a simple dynamical system to simulate this response and showed that it resembles observations of mesohighs and wake lows. We found that when the cooling is defined to be three-dimensional, to move and to dissipate after six hours, like the stratiform cooling of a typical squall system, the buoyancy-wave response includes a mesohigh and a wake low which not only have a realistic wind and pressure structure but also exhibit a realistic life cycle. Using mathematics we showed that the mature mesohigh-wake-low couplet may be interpreted as a quasi-steady-state response to a moving forcing.

Our interpretation of mesohighs and wake lows is for the most part compatible with those put forward in previous studies. It is consistent with the generally accepted idea that mesohighs and wake lows are hydrostatic manifestations of lower tropospheric temperature anomalies. It also weaves together past explanations of the subsidence responsible for the wake low. Miller and Betts (1977) suggested that the low-level subsidence in the wake of convective systems was dynamically driven by the spreading of cool air near the surface. Within the simulations presented here the horizontal inertia of the low-level divergent flow and the mid-level convergent flow drives the subsidence. Johnson and Hamilton (1988) connected the subsidence to system-relative rear-inflow in the mid-troposphere. The buoyancy waves which are responsible for the mesohighs and wake lows simulated here also cause perturbations to the wind field which can explain the rear inflow (Pandya and Durran 1996). Gallus (1996) showed that microphysical processes within the stratiform region alone can generate the subsidence responsible for the wake low. Within the simulations presented here the only forcing is the low-level cooling associated with stratiform precipiation. Schmidt and Cotton (1990) also attributed the subsidence above the wake low to a buoyancy-wave, but within their simulation this subsidence was much deeper and may have been caused by deep convective heating. One aspect of the mesohigh which is discussed here that is not emphasized in other studies is that the coolness of the lower troposphere above it may be more a consequence of vertical motion than of local forcing.

Because of their ideal nature, the simulations presented here have a number of limitations. One such limitation is that they occur in an environment with no wind shear. Many MCS's have significant low-level shear in their vicinity. Schmidt and Cotton (1990) tested the sensitivity of buoyancy-wave circulations within a squall system to wind shear. They found that similar waves form in environments with and without shear, and that the phase speed of the waves which form in shear is shifted by the mean velocity through the depth of the wave. A second limitation of the simulations presented here is that they neglect nonlinear terms, so that nonlinear phenomenon such as gravity currents are not represented. A third limitation is that the bouyancy frequency N was assumed to be constant with respect to height. This assumption was made so that the vertical structure functions of the solution would be sines and cosines. When N is allowed to vary these functions still resemble trigonometric functions (e.g., Haertel and Johnson 1998).

While the interpretation of mesohighs and wake lows presented here has limitations because of its ideal nature, it is powerful for the same reason. The mathematics and the physical principles are so simple that they could be communicated to graduate students in a single lecture. Perhaps because of its simplicity the interpretation will endure.

REFERENCES

Ely, G. F., 1982: Case study of a significant thunderstorm wake deprression along the Texas coast: May 29-30 1981. NOAA Tech. Memo. NWS SR-105 64 pp.

Fujita, T. T., 1955: Results of detailed synoptic studies of squall lines. *Tellus,* **4,** 405-436.

Fujita, T. T., 1959: Precipitation and cold air production in mesoscale thunderstorm systems. *J. Meteor.,* **16,** 454-466.

Fujita, T. T., 1963: Analytical mesometeorology. A review. *Meteor. Monogr.,* **5,** 77-125.

Gallus, W. A., Jr., 1996: The influence of microphysics in the formation of intense wake lows: a numerical modeling study. *Mon. Wea. Rev.,* **124,** 2267-2281.

Gallus, W. A., Jr. and R. H. Johnson, 1991: Heat and moisture budgets of an intense midlatitude squall line. *J. Atmos. Sci.,* **48,** 122-146.

Geisler, 1970: Linear theory of the response of a two layer ocean to a moving hurricane. *Geophysical Fluid Dynamics,* **1,** 249-272.

Haertel, P. T. and R. H. Johnson, 1998: Two-day disturbances in the equatorial western Pacific. *Quart. J. R. Met. Soc.,* **124** , 615-636.

Holton, J. R., 1992: An Introduction to Dynamic Meteorology. Academic Press, San Diego, 511pp.

Hane, C. E. and P. S. Ray, 1985: Pressure and buoyancy fields derived from Doppler radar data in a tornadic thunderstorm. *J. Atmos. Sci.,* **42,** 18-35.

Hertenstein, R. F. and W. H. Schubert, 1991: Potential vorticity anomalies associated with squall lines. *Mon. Wea. Rev.,* **119,** 1663-1672.

Houze, R. A., Jr., 1982: Cloud clusters and large-scale vertical motions in the tropics. *J. Meteorol. Soc. Jpn.,* **60,** 396-410.

Houze, R. A., Jr., B. F. Smull, and P. Dodge, 1990: Mesoscale organization of springtime rainstorms in Oklahoma. *Mon. Wea. Rev.,* **118,** 613-654.

Johnson, R. H. and S. Chen, and J. J. Toth, 1989: Circulations associated with a mature-to-decaying midlatitude mesoscale convective system. Part I: Surface features--heat bursts and mesolow development. *Mon. Wea. Rev.,* **117,** 942-959.

Johnson, R. H., and P. J. Hamilton, 1988: The relationship of surface pressure features to the precipitation and airflow structure of an intense midlatitude squall line. *Mon. Wea. Rev.,* **116,** 1444-1472.

Lin, Y. L. and R. B. Smith, 1986: Transient dynamics of airflow near a local heat source. *J. Atmos. Sci.,* **43,** 40-49.

Loehrer, S. M. and R. H. Johnson, 1995: Surface pressure and precipitation life cycle characteristics of PRE-STORM mesoscale convective systems. *Mon. Wea. Rev.,* **123,** 600-621.

Meuse, C., L. Galusha, M. Isaminger, M. Moore, D. Rhoda, F. Robasky, and M. Wolfson, 1996: Analysis of the 12 April 1996 wind shear incident at DFW airport. Preprints, Workshop on Wind Shear and Wind Shear Alert Systems, Amer. Meteor. Soc., Oklahoma City, 23-33.

Miller, M. J. and A. K. Betts, 1977: Traveling convective storms over Venezuela. *Mon. Wea. Rev.,* **105,** 833-848.

Nicholls, M. E., R. A. Pielke and W. R. Cotton, 1991: Thermally forced gravity waves in an atmosphere at rest. *J. Atmos. Sci.,* **48,** 1869-1884.

Pandya, R., D. Durran, and C. Bretherton, 1993: Comments on "thermally forced gravity waves in an atmosphere at rest." *J. Atmos. Sci.,* **50,** 4097-4102.

Pandya, R. E. and D. R. Durran, 1996: The influence of convectively generated thermal forcing on the mesoscale circulations around squall lines. *J. Atmos. Sci.,* **53,** 2924-2951.

Papoulis, A., 1962: The Fourier Integral and its Applications. McGraw-Hill, New York, 318pp.

Pedgley, D. E., 1962: A meso-synoptic analysis of the thunderstorms on 28 August 1958. *Brit. Meteor. Off. Geophys. Mem.,* **No. 106,** 74 pp.

Rotunno, R., J. B. Klemp and M. L. Weismann, 1988: A theory for strong, long-lived squall lines. *J. Atmos. Sci.,* **45,** 463-485.

Sanders, F. and K. A. Emanuel, 1997: The momentum budget and temporal evolution of a mesoscale convective system. *J. Atmos. Sci.* **34,** 322-330.

Schaffer, W., 1947: The thunderstorm high. *Bull. Amer. Meteor. Soc.,* **28,** 351-355.

Schmidt, J. M. and W. R. Cotton, 1989: A high plains squall line associated with severe surface winds. *J. Atmos. Sci.,* **46,** 281-302.

Schmidt J. M. and W. R. Cotton, 1990: Interactions between upper and lower tropospheric gravity waves on squall line structure and maintenance. *J. Atmos. Sci.,* **47,** 1205-1222.

Smull, B. F. and D. P. Jorgensen, 1990: Pressure and buoyancy perturbations near an intense wake low in a midlatitude mesoscale convective system. /fI Extended Abstracts, 4th Conf. on Mesoscale Processes.

Stumpf, G. J., R. H. Johnson and B. F. Smull, 1991: The wake low in a midlatitude convective system having complex convective organization. *Mon. Wea. Rev.,* **119,** 134-158.

Williams, D. T., 1963: The thunderstorm wake of May 4, 1961. Natl. Severe Storms Project Rep. No. 18, U.S. Dept. of Commerce, Washington DC, 23 pp. [NTIS PB 168223].

Zhang, Da-Lin and Kun Gau, 1989: Numerical simulation of an intense squall line during 10-11 June 1985 PRE-STORM. Part II: Rear inflow, surface pressure perturbations and stratiform precipitation. *Mon. Wea. Rev.,* **117,** 2067-2093.